

Contents

	Page
Title page	i
Abstract	iii
Résumé	v
List of Publications	ix
List of Figures	xi
List of Tables	xvii
1 Introduction	1
1.1 A brief history of superfluidity	1
1.2 Some key concepts	3
1.2.1 Bose-Einstein condensation and long-range order	4
1.2.2 Bogolyubov's approximation	5
1.2.3 Landau's criterion for superfluidity	7
1.2.4 Rotation and vorticity in superfluids	8
1.3 Helium droplets	11
2 The DFT method for heavy impurities	15
2.1 The Kohn-Sham approach	16
2.2 Time-dependent DFT	17
2.3 The Orsay-Trento Density Functional	18
2.4 The Solid-OT Density Functional	20
2.5 Static calculations	21
2.5.1 Producing vortical states	22
2.5.2 Technical details on how the static equations are solved	23
2.6 Dynamic calculations	23
2.6.1 Diatomics in Molecules	23
2.6.2 Including spin-orbit coupling	25
2.6.3 Absorbing potential at the box boundaries	27
2.6.4 Technical details on how the dynamic equations are solved	27

Part I Photo-excitation dynamics of alkalis	29
3 Alkali-doped nanodroplets	31
4 Imaging Excited-State Dynamics	35
5 Desorption dynamics of RbHe exciplexes	43
6 Supervised work: potassium-doped nanodroplets	59
Part II Capture by quantised vortices	61
7 Quantised vortices in droplets	63
8 Head-on collisions of Xe and Cs	67
8.1 Introduction	67
8.2 Results	68
9 Capture by He droplets hosting quantised vortices	75
9.1 Introduction	75
9.2 Xe capture by vortex-free droplets	81
9.3 Helium droplets hosting vortex lines	83
9.4 Dynamics of Xe and Ar capture by vortex lines	86
9.5 Vortex arrays in ^4He droplets doped with Ar atoms	88
10 To conclude	101
A Angular velocity and angular momentum	105
Bibliography	109
Acknowledgements	121
Résumé étendu en français	123

2

The DFT method for heavy impurities

One Functional to rule them all,
One Functional to find them,
One Functional to bring them all
and in a droplet bind them.

F.M.G.J. Coppens

From a theoretical point of view, superfluid helium must be considered as a high dimensional quantum system. Quantum Monte Carlo^[56] (QMC) and direct quantum mechanical^[57-59] calculations are the most accurate methods, but their computational demand quickly exceeds currently available computer resources when the number of helium atoms increases. Furthermore, QMC cannot describe dynamic evolution of superfluid helium in real time. To address these limitations, semi-empirical methods based on density functional theory (DFT) formalism have been introduced^[7,8,60]. DFT can be applied to much larger systems than QMC and allows for time-dependent formulation. As such, it offers a good compromise between accuracy and computational feasibility. The main drawback of DFT is that the exact energy functional is not known and must therefore be constructed in a semi-empirical manner. Moreover, doped helium droplets are limited to a mean-field description of the dopant-helium interaction. Nevertheless, DFT is the only method to date that can successfully reproduce results from a wide range of time-resolved experiments in superfluid helium, for realistic sizes compared to experimental conditions.

2.1 The Kohn-Sham approach

The starting point for the density functional method is the Hohenberg-Kohn (HK) theorem^[61], which states that the ground-state energy E_v of an *interacting inhomogeneous* system in a static potential v can be written in as a unique functional of the one-body density ρ as

$$E_v[\rho] = \int v(\mathbf{r})\rho(\mathbf{r}) \, d\mathbf{r} + F[\rho] \quad (2.1)$$

where $F[\rho]$ is a universal functional—valid for *any* number of particles and *any* external potential v —of the one-body density, defined as

$$\rho(\mathbf{r}) := \langle \Phi | \hat{\rho}(\mathbf{r}) | \Phi \rangle = \left\langle \Phi \left| \sum_{i=1}^N \delta(\mathbf{r} - \mathbf{r}_i) \right| \Phi \right\rangle \quad (2.2)$$

and $\Phi(\mathbf{r}_1, \mathbf{r}_2, \dots, \mathbf{r}_N)$ is the many-body wave function of such a system. Furthermore, the functional $F[\rho]$ gives the ground state energy *if and only if* the input density is the true ground state density of the system.

Kohn and Sham (KS) later reformulated^[62] the theory by introducing an approximation scheme for the functional $F[\rho]$ that is analogous to Hartree's method, but also contains the major part of the correlation effects inherent in interacting many-body systems. The approximation starts by defining

$$F[\rho] := T[\rho] + E_c[\rho] \quad (2.3)$$

where $T[\rho]$ is now the kinetic energy of a fictitious system of *non-interacting* particles with density ρ and $E_c[\rho]$ is the interaction term of an *interacting* system with the same density, which contains all the other terms of the functional. For the kinetic part this allows us to write the total kinetic energy $T[\rho]$ as the sum of the individual kinetic energies T_i of the non-interacting particles

$$T = \sum_i T_i = -\frac{\hbar^2}{2m_4} \sum_i \langle \varphi_i | \nabla^2 | \varphi_i \rangle = -\frac{\hbar^2}{2m} \sum_i \int \varphi_i^*(\mathbf{r}) \nabla^2 \varphi_i(\mathbf{r}) \, d\mathbf{r}, \quad (2.4)$$

where m_4 is the mass of a ${}^4\text{He}$ atom and the $\{\varphi_i\}$ are the Kohn-Sham single-particle orbitals corresponding to the many-body KS wave function $\Phi_{\text{KS}}(\mathbf{r}_1, \mathbf{r}_2, \dots, \mathbf{r}_N) = \prod_i \varphi_i(\mathbf{r}_i)$ and leading to the density (using the definition in Equation (2.2)) $\rho(\mathbf{r}) = \sum_i |\varphi_i(\mathbf{r})|^2$.

There is difference between the true kinetic energy of the interacting system and the fictitious one, due to the neglecting of the correlations. This difference is being corrected and accounted for in the correlation energy $E_c[\rho]$.

Because the functional we used in this work is calibrated to produce the correct behaviour of bulk liquid helium at zero temperature $T = 0$ and zero pressure $P = 0$, we assume complete Bose-Einstein (BE) condensation of the helium. In this case all the

helium atoms occupy the same single-particle KS-orbital φ_0 . Therefore the many-body wave function and the density simplifies further to

$$\Phi_{BEC}(\mathbf{r}_1, \mathbf{r}_2, \dots, \mathbf{r}_N) = \prod_i \varphi_0(\mathbf{r}_i) \quad (2.5)$$

and

$$\rho(\mathbf{r}) = N |\varphi_0(\mathbf{r})|^2 \quad (2.6)$$

respectively. As explained in Section 1.2.2, it is customary to define an effective wave function

$$\Psi(\mathbf{r}) := \sqrt{\rho(\mathbf{r})} = \sqrt{N} \varphi_0(\mathbf{r}) \quad (2.7)$$

for the condensate (see Equation (1.12)), which is sometimes called a *macroscopic wave function* or *order parameter*. We can now simplify the expression for the kinetic energy (Equation (2.4))

$$T = -\frac{\hbar^2}{2m_4} N \int \varphi_0^*(\mathbf{r}) \nabla^2 \varphi_0(\mathbf{r}) \, d\mathbf{r} = \frac{\hbar^2}{2m_4} N \int |\nabla \varphi_0|^2 \, d\mathbf{r}, \quad (2.8)$$

where we used partial integration to get to the last step and imposed that the orbital φ_0 vanishes at the boundaries. With our definition Equation (2.7) we can now write the kinetic energy as a functional of the density

$$T[\rho] = \frac{\hbar^2}{2m_4} \int |\nabla \sqrt{\rho}|^2 \, d\mathbf{r} \quad (2.9)$$

To summarise, we write the complete energy functional E_v as

$$E_v[\rho] = \int v(\mathbf{r}) \rho(\mathbf{r}) \, d\mathbf{r} + \frac{\hbar^2}{2m_4} \int |\nabla \sqrt{\rho}|^2 \, d\mathbf{r} + \int \mathcal{E}_c[\rho] \, d\mathbf{r} \quad (2.10)$$

where we defined the correlation energy density functional \mathcal{E}_c through

$$E_c[\rho] := \int \mathcal{E}_c[\rho] \, d\mathbf{r}. \quad (2.11)$$

The difficult job is to design a functional \mathcal{E}_c such that the desired physical properties of helium can be recovered. This is far from trivial but several of these density functionals are available now. The one used in this work is discussed in Section 2.3.

2.2 Time-dependent DFT

To describe the time evolution of the system, the Runge-Gross theorem extends DFT to its time-dependent version TDDFT^[63]. The functional variation of the associated action (see Equation (2.49) for an example) leads to the following time-dependent Euler-Lagrange (EL) equation

$$i\hbar \frac{\partial}{\partial t} \Psi(\mathbf{r}, t) = \left\{ -\frac{\hbar^2}{2m_4} \nabla^2 + \frac{\delta \mathcal{E}_c}{\delta \rho} \right\} \Psi(\mathbf{r}, t) := \mathcal{H}[\rho] \Psi(\mathbf{r}, t) \quad (2.12)$$

Table 2.1: Model parameters for the OT-DFT and solid functionals.

ϵ_{LJ} (K)	σ (Å)	h (Å)	c_2 (K Å ⁶)	c_3 (K Å ⁹)	α_s (Å ³)
10.22	2.556	2.190323	-2.41186×10^4	1.85850×10^6	54.31
ρ_{0s} (Å ⁻³)	l (Å)	C (Hartree)	β (Å ³)	ρ_m (Å ⁻³)	γ_{11}
0.04	1.	0.1	40.	0.37	-19.7544
γ_{12} (Å ⁻²)	α_1 (Å ⁻²)	γ_{21}	γ_{22} (Å ⁻²)	α_2 (Å ⁻²)	
12.5616	1.023	-0.2395	0.0312	0.14912	

As long as we are in the thermodynamic regime the solutions $\Psi(\mathbf{r}, t)$ can be decomposed into the liquid density and associated velocity potential field (see Section 1.2.2 and Section 1.2.4).

Considering only eigenstates $\Psi(\mathbf{r}, t) = \Psi_0(\mathbf{r}) e^{-i\mu t/\hbar}$ of the time independent Hamiltonian $\mathcal{H}[\rho]$ the time-dependent EL-equation reduces to a time independent one

$$\left\{ -\frac{\hbar^2}{2m_4} \nabla^2 + \frac{\delta \mathcal{E}_c}{\delta \rho} \right\} \Psi_0(\mathbf{r}) = \mu \Psi_0(\mathbf{r}) \quad (2.13)$$

with μ the chemical potential. Solving this equation by iteration will result in the ground state density $|\Psi_0|^2$ of the system. Within the HK-framework and the variation principle that was used to obtain these EL-equations, the nature of the minimisation is such that it gives the lowest energy for a given symmetry. This means that as long as the input state does not break the symmetry of the time-independent EL-equation, it minimises the energy of this state even if it does not lead to the ground state. This can be used to obtain a stationary vortex-line solution. With the inclusion of appropriate constraints in the energy functional the same procedure can be used to obtain helium densities with an array of vortex-lines.

2.3 The Orsay-Trento Density Functional

The functional that is used in the work presented in this thesis is based on the Orsay-Trento (OT) functional^[5]. It uses a finite-range, non-local approach and it is, to date the most accurate model in the sense that its parameters were fitted to reproduce the bulk

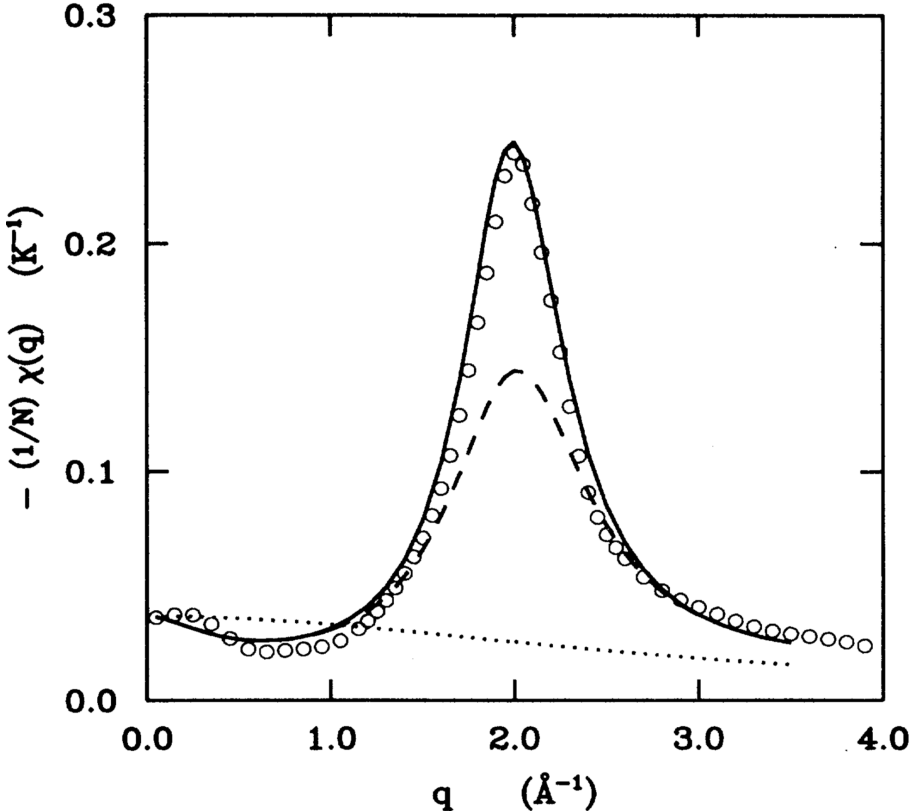


Figure 2.1: Static response $-\chi$ (see Ref. [5], Eqn. (11)) per atom of liquid ${}^4\text{He}$ at zero pressure. Points: experimental data; dotted line: from the functional of Refs. [7, 8]; dashed line: Orsay-Paris (OP) functional^[9]; solid line: OT functional.

properties of liquid helium at $T = 0 = P$. It is written as

$$\begin{aligned} \mathcal{E}_c[\rho, \mathbf{v}] = & \frac{1}{2} \int \left\{ \rho(\mathbf{r}) V_{LJ}(|\mathbf{r} - \mathbf{r}'|) \rho(\mathbf{r}') \right. \\ & + \frac{1}{2} c_2 \rho(\mathbf{r}) [\bar{\rho}(\mathbf{r})]^2 + \frac{1}{3} c_3 \rho(\mathbf{r}) [\bar{\rho}(\mathbf{r})]^3 \Big\} d\mathbf{r}' \\ & - \frac{\hbar^2}{4m_4} \alpha_s \int F(|\mathbf{r} - \mathbf{r}'|) \left[1 - \frac{\tilde{\rho}(\mathbf{r})}{\rho_{0s}} \right] \nabla \rho(\mathbf{r}) \cdot \nabla \rho(\mathbf{r}') \left[1 - \frac{\tilde{\rho}(\mathbf{r}')}{\rho_{0s}} \right] d\mathbf{r}' \\ & - \frac{m_4}{4} \int V_J(|\mathbf{r} - \mathbf{r}'|) \rho(\mathbf{r}) \rho(\mathbf{r}') [\mathbf{v}(\mathbf{r}) - \mathbf{v}(\mathbf{r}')]^2 d\mathbf{r}' \end{aligned} \quad (2.14)$$

The first term corresponds to a classical Lennard-Jones type two-body interaction between helium atoms. The interaction is screened at short distances where the interaction energy is of the same order as the correlation effects:

$$V_{LJ}(r) = \begin{cases} \epsilon_{LJ} \left[\left(\frac{\sigma}{r} \right)^{12} - \left(\frac{\sigma}{r} \right)^6 \right] & \text{if } r > h \\ 0 & \text{otherwise} \end{cases} \quad (2.15)$$

In the second line, the terms corresponding to c_2 and c_3 , correct for short range correlations when $r < h$. The weighted density $\bar{\rho}$ is the average density ρ over a sphere of radius

h :

$$\bar{\rho}(\mathbf{r}) = \int \Pi_h(|\mathbf{r} - \mathbf{r}'|) \rho(\mathbf{r}') d\mathbf{r}', \quad (2.16)$$

with

$$\Pi_h(r) := \begin{cases} \frac{3}{4\pi h^3} & \text{if } r \leq h \\ 0 & \text{otherwise} \end{cases} \quad (2.17)$$

The third line is a non-local correction to the kinetic energy (KC). It partially accounts for the difference $\mathcal{T}[\rho] - T[\rho]$ mentioned in Section 2.1. The gradient-gradient interaction function F is a Gaussian kernel defined as

$$F(r) = \frac{1}{l^3 \sqrt{\pi^3}} e^{-r^2/l^2} \quad (2.18)$$

All the parameters are fitted to reproduce the peak of the static response function (see Figure 2.1) in the bulk liquid. The factor $(1 - \tilde{\rho}/\rho_{0s})$ is included to match the pressure dependence of the static response function predicted by diffusion Monte Carlo calculations^[64]. The quantity $\tilde{\rho}(\mathbf{r})$ is another weighted density, calculated using F as a weight

$$\tilde{\rho}(\mathbf{r}) := \int F(|\mathbf{r} - \mathbf{r}'|) \rho(\mathbf{r}') d\mathbf{r}' \quad (2.19)$$

The density $\tilde{\rho}(\mathbf{r})$ is very close to the normal density $\rho(\mathbf{r})$ except in very inhomogeneous situations. For pure helium droplets and free helium surfaces one can safely use ρ instead of $\tilde{\rho}$. In the presence of significant short-range density oscillations, e.g. in the presence of heavy atomic impurities as presented in this thesis or electrons, the helium density needs to be smoothed by the Gaussian kernel F .

Finally, the last line in Equation (2.14) is called the *back-flow* term and influences the dynamic response of the system. It plays the role of a non-local kinetic energy. Since the back-flow contains the factor $\mathbf{v} - \mathbf{v}'$, with \mathbf{v} defined in Equation (1.24), the contribution will only be non-zero whenever the effective wave function Ψ is complex-valued. Consequently, for time-independent cases it means that this will only affect the vortex states. The phenomenological effective current-current interaction $V_J(r)$ is calibrated so that it reproduces the experimental phonon-roton spectrum (see Figure 1.3):

$$V_J(r) = (\gamma_{11} + \gamma_{12} r^2) e^{-\alpha_1 r^2} + (\gamma_{21} + \gamma_{22} r^2) e^{-\alpha_2 r^2} \quad (2.20)$$

All the parameters of the functional are given in Table 2.1.

2.4 The Solid-OT Density Functional

In the presence of highly inhomogeneous liquid densities, e.g. atomic impurities with a very strong He-X interaction, the OT-functional Equation (2.14) becomes numerically

unstable. To deal with this problem an additional cut-off can be used

$$\mathcal{E}^{\text{sol}} := C \rho(\mathbf{r}) \{1 + \tanh(\beta[\rho(\mathbf{r}) - \rho_m])\} \quad (2.21)$$

where the model parameters $\{C, \beta, \rho_m\}$ are specified in Table 2.1. Including this term in the OT-functional prevents excessive density build-up. \mathcal{E}^{sol} only starts to deviate from zero whenever the liquid density ρ is comparable to ρ_m or larger. Therefore, inclusion of this term in the functional does not alter the density distribution. This penalty term was originally developed to account for the liquid-solid phase transition of ${}^4\text{He}$ ^[65,66]. The functional that has been used to obtain the result presented in this work is referred to as the “Solid-OT-DFT functional”. It consists of the first three terms of the original OT-functional Equation (2.14), plus \mathcal{E}^{sol}

$$\begin{aligned} \mathcal{E}_c^{\text{sol}}[\rho] = & \frac{1}{2} \int \left\{ \rho(\mathbf{r}) V_{LJ}(|\mathbf{r} - \mathbf{r}'|) \rho(\mathbf{r}') \right. \\ & + \frac{1}{2} c_2 \rho(\mathbf{r}) [\bar{\rho}(\mathbf{r})]^2 + \frac{1}{3} c_3 \rho(\mathbf{r}) [\bar{\rho}(\mathbf{r})]^3 \left. \right\} d\mathbf{r}' \\ & + C \rho(\mathbf{r}) \{1 + \tanh(\beta[\rho(\mathbf{r}) - \rho_m])\} \end{aligned} \quad (2.22)$$

2.5 Static calculations

In the work presented here all the impurities are heavy compared to the mass of ${}^4\text{He}$, e.g. the mass of rubidium (Rb) is about 21 times larger than that of helium (He), xenon (Xe) roughly 33 times and argon (Ar) about 10 times. Therefore we are allowed to treat the centre of mass motion of the impurities as classical. It was also checked for potassium (K) which is slightly lighter than Ar^[10]. In the functional this will be modelled as an external field V_X , the impurity-He pair interaction

$$E[\rho] \rightarrow E[\rho] + \int \rho(\mathbf{r}) V_X(|\mathbf{r} - \mathbf{r}_I|) d\mathbf{r} \quad (2.23)$$

where \mathbf{r}_I is the location of the impurity. Varying the modified functional to minimise the energy one now finds a new EL-equation in which the helium-impurity interaction is included:

$$ngbank \quad (2.24)$$

This equation is then solved by iteration in a self-consistent way by the imaginary time propagation method^[67] (ITM) in cartesian coordinates. The calculations are performed in three dimensions without imposing any symmetries that are present in the external potential. All the quantities are discretised on an evenly spaced Cartesian grid with a step-size that is typically of the order of 0.4 Å. This value is chosen small enough such that the corresponding maximum momentum in Fourier-space is high enough compared to the helium momenta involved in the dynamics. The differential operators are evaluated

using a k -point finite difference method where in most applications $k = 13$ is sufficiently accurate. The integrals in the density-functional can be expressed as convolutions and can therefore be evaluated in momentum-space by exploiting the convolution theorem, using proprietary highly optimised parallel Fast Fourier Transform algorithms.

2.5.1 Producing vortical states

The helium density that minimises the energy of the vortical states Ψ_s

$$\Psi_s(\mathbf{r}) = \sqrt{\rho(r, z)} e^{is\varphi} \quad (2.25)$$

introduced in Section 1.2.4, can be obtained by solving the same EL-equation as for a vortex-free droplet. This becomes clearer when we write Equation (2.13) in cylindrical coordinates:

$$\left\{ -\frac{\hbar^2}{2m_4} \left[\frac{1}{r} \frac{\partial}{\partial r} \left(r \frac{\partial}{\partial r} \right) - \frac{s^2}{r^2} + \frac{\partial^2}{\partial z^2} \right] + \frac{\delta E_c}{\delta \rho} \right\} \Psi_s(\mathbf{r}) = \mu \Psi_s(\mathbf{r}) \quad (2.26)$$

Written like this it is evident that the ground state Ψ_0 is just the special case for $s = 0$. Obtaining the solution using the ITM works as long as the solution has overlap with initial guess for the order parameter. Starting with a trial order parameter similar to Ψ_s will guarantee this. To do this we apply the “imprinting” technique where we apply the ground state density of a previously obtained vortex-free droplet and multiply it with a normalised complex factor

$$\Psi(\mathbf{r}) = \sqrt{\rho_0(x, y, z)} \times \frac{x + iy}{\sqrt{x^2 + y^2}} \quad (2.27)$$

where ρ_0 is the ground state density of the vortex-droplet. In cylindrical coordinates this factor is equivalent to the one in Equation (1.25) for $s = 1$.

This changes for droplets with two or more vortices, where the cylindrical symmetry is broken and the solutions are no longer solutions of Equation (2.26), nor eigenfunctions of the angular momentum operator. In this case the time-independent EL-equation has to be modified to include a rotational constraint solution in the co-rotating frame

$$\mathcal{H} \rightarrow \mathcal{H} - \Omega \hat{L}_z \quad (2.28)$$

such that for a suitable choice of Ω the vortex-array solution becomes favourable to the ground state and also to excited states with angular momentum $s \geq 2$. Since these states are no longer eigenstates of the original time-dependent Hamiltonian, these states are no longer stationary and will start to rotate with frequency Ω . The initial guess for a droplet with n_v vortices can be produced using the same imprinting method as mentioned before

$$\Psi(\mathbf{r}) = \sqrt{\rho_0(x, y, z)} \times \prod_{j=1}^{n_v} \left[\frac{(x - x_j) + i(y - y_j)}{\sqrt{(x - x_j)^2 + (y - y_j)^2}} \right] \quad (2.29)$$

where ρ_0 is again the ground state density of the vortex-free droplet and (x_j, y_j) is the initial position of the j -th vortex-line parallel to the z -axis.

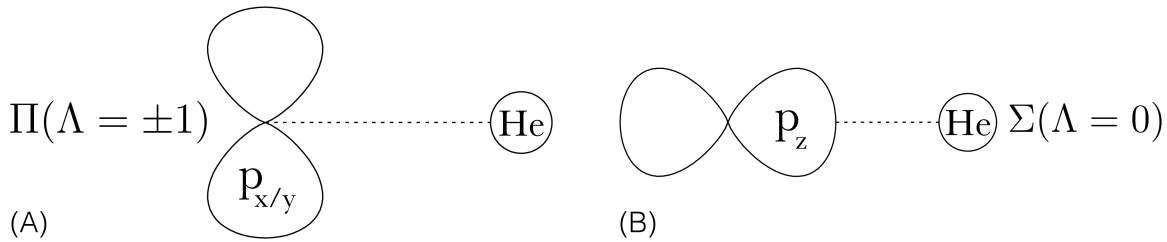


Figure 2.2: Level splitting of the p-orbitals in the presence of helium, that breaks the spherical symmetry. (A) A double degenerate $n'p_{x/y}$ -orbital and (B) a single $n'p_z$ -orbital. (Illustration courtesy of M. Martinez^[10].)

2.5.2 Technical details on how the static equations are solved

2.6 Dynamic calculations

For the dynamic evolution of atomic impurities excited from ns -states to $n's$ -states, we do not need to keep track of the evolution of the electronic state of the impurity since it keeps its spherically symmetric orbital. In this case we only need to describe the time evolution of the centre of mass coordinate of the impurity. As in the statics, because of the large atomic mass of the impurity compared to helium, the time evolution of the centre of mass coordinate of the impurity is treated classically. To obtain the correct energy for the whole droplet-impurity system the energy functional needs to be extended to include the impurity's centre of mass motion and the impurity-helium interaction

$$E[\rho] \rightarrow E[\rho] + \frac{1}{2}m_I \dot{\mathbf{r}}_I^2 + \int \rho(\mathbf{r}) V_{X^*}(|\mathbf{r} - \mathbf{r}_I|) d\mathbf{r} \quad (2.30)$$

where the second term on the right is the classical kinetic energy of the impurity (which was not present in the static case, Equation (2.23)), $\dot{\mathbf{r}}_I$ is the time derivative of the impurity location, m_I is the impurity mass and V_{X^*} is the impurity-He pair interaction potential for an impurity in the ground-, excited $n's$ - or ionised state. The equations of motion for the time evolution of the effective wave function $\Psi(\mathbf{r}, t)$ and the second time derivative of the impurity location $\ddot{\mathbf{r}}_I$ are

$$\begin{aligned} i\hbar \frac{\partial}{\partial t} \Psi &= \left[-\frac{\hbar^2}{2m_4} \nabla^2 + \frac{\delta \mathcal{E}_c}{\delta \rho} + V_{X^*}(|\mathbf{r} - \mathbf{r}_I|) \right] \Psi \\ m_I \ddot{\mathbf{r}}_I &= -\nabla_{\mathbf{r}_I} \left[\int \rho(\mathbf{r}) V_{X^*}(|\mathbf{r} - \mathbf{r}_I|) d\mathbf{r} \right] \\ &= - \int V_{X^*}(|\mathbf{r} - \mathbf{r}_I|) \nabla \rho(\mathbf{r}) d\mathbf{r} \end{aligned} \quad (2.31)$$

2.6.1 Diatomics in Molecules

The situation becomes more complicated for ns -states excited to $n'p$ -states (effective one-electron excited 2P -states). Since the three p-orbitals are no longer spherically sym-

metric and start mixing due to the interaction with the He droplet and spin-orbit coupling, we also need to include a description that accounts for the mixing of these orbitals in a dynamic way. To do this we use Diatomics in Molecules^[68](DIM). The interaction between a helium atom (1S_0 -state) and the triply degenerate $L = 1$ electronic state of the impurity partially lifts the degeneracy so that the interaction can be decomposed into a Σ -state and a doubly degenerate Π -state (see Figure 2.2). In the cylindrical symmetry it is customary to use the molecular term symbol ${}^{2S+1}\Lambda_\Omega$ to label the levels. In the bound region of the potentials S is the electronic spin angular momentum (and $2S + 1$ the spin multiplicity), Λ is the quantum number for the projection of the electronic orbital angular momentum and Ω is the total electronic angular momentum, along the internuclear axis. Or symbolically

$$m_j = m_l + m_s \longrightarrow \Omega = \Lambda + m_s \quad (2.32)$$

Following the spectroscopic notation the orbitals corresponding to $\Lambda = 0, 1, 2, 3, \dots$ are labeled $\Sigma, \Pi, \Delta, \Phi, \dots$. The state vector of the impurity interacting with a He atom can be expressed in an uncoupled basis

$$|p_{im}\rangle \in \{|p_{xm}\rangle, |p_{ym}\rangle, |p_{zm}\rangle\} \quad (2.33)$$

of real one-electron p-orbitals oriented along the internuclear axis (see Figure 2.3). The helium-impurity interaction matrix is given by

$$\begin{aligned} \mathcal{V}^{DIM}(r_m) &= V_\Pi(r_m)(|p_{xm}\rangle\langle p_{xm}| + |p_{ym}\rangle\langle p_{ym}|) + V_\Sigma(r_m)|p_{zm}\rangle\langle p_{zm}| \\ &= V_\Pi(r_m)(\mathbb{1}_3 - |p_{zm}\rangle\langle p_{zm}|) + V_\Sigma(r_m)|p_{zm}\rangle\langle p_{zm}| \\ &= V_\Pi(r_m)\mathbb{1}_3 + [V_\Sigma(r_m) - V_\Pi(r_m)]|p_{zm}\rangle\langle p_{zm}| \end{aligned} \quad (2.34)$$

where r_m is the modulus of the interatomic separation vector and V_Π and V_Σ are the Π and Σ impurity-He pair potentials in the absence of spin-orbit coupling. For a system consisting of N helium atoms the total interaction energy is calculated by summing over all the contributions of the N individual ${}^4\text{He}$ -X contributions

$$\mathcal{U}^{DIM}(\mathbf{r}_I) = \sum_{m=1}^N \mathcal{V}^{DIM}(r_m) \quad (2.35)$$

It is more convenient to express the interaction in a basis common to all impurity-helium pairs, instead of a basis that depends on the particular impurity-helium pair chosen. To do this we apply a rotation $\mathcal{R}_m : \hat{\mathbf{z}}_m \mapsto \hat{\mathbf{z}} \propto \mathbf{r}_I$, so that the matrix corresponding to the m^{th} ${}^4\text{He}$ atom expressed in the common basis is given by

$$|p_{zm}\rangle\langle p_{zm}| = \mathcal{R}_m |p_z\rangle\langle p_z| \mathcal{R}_m^{-1} \quad (2.36)$$

It can be shown that the elements of this matrix in cartesian coordinates are of the form

$$\langle p_i | \mathcal{R}_m | p_z \rangle\langle p_z | \mathcal{R}_m^{-1} | p_j \rangle = \frac{r_{im} r_{jm}}{\|\mathbf{r}_m\|^2} \quad (2.37)$$

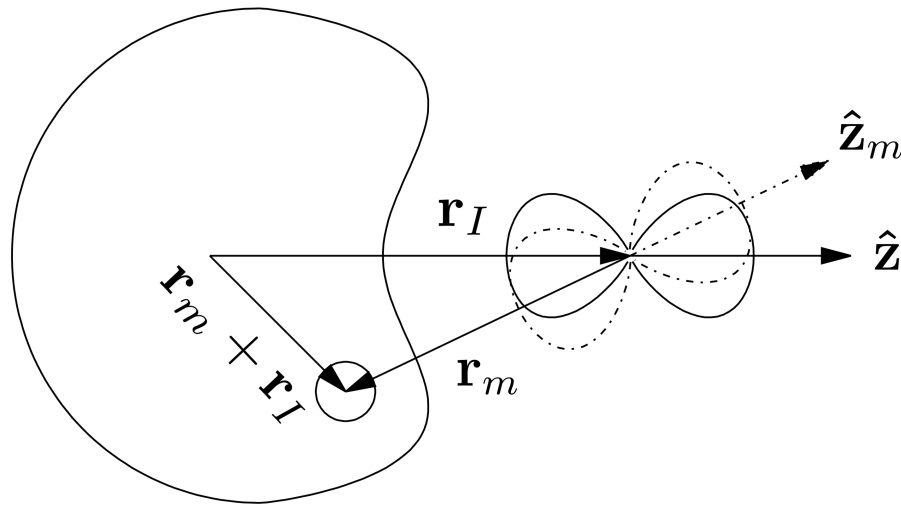


Figure 2.3: The set of axis defined in the DIM description. (Illustration courtesy of M. Martinez^[10].)

where $(i, j) \in \{x, y, z\}$. With these definitions we can write the matrix elements U_{ij}^{DIM} of the interaction energy \mathcal{U}^{DIM}

$$U_{ij}^{DIM}(\mathbf{r}_I) = \langle p_i | \mathcal{U}^{DIM} | p_j \rangle = \sum_{m=1}^N V_{ij}^{DIM}(r_m) \quad (2.38)$$

where

$$V_{ij}^{DIM}(r_m) := V_{\Pi}(r_m) \delta_{ij} + \left[V_{\Sigma}(r_m) - V_{\Pi}(r_m) \right] \frac{r_{im} r_{jm}}{\|\mathbf{r}_m\|^2} \quad (2.39)$$

are the matrix elements of \mathcal{V}^{DIM} expressed in the common basis. Since we are working with a continuous helium density $\rho(\mathbf{r})$ and not with discrete atoms, the summation over N helium atoms in the previous expression is replaced by an integral over the density $\sum_m \rightarrow \int \rho(\mathbf{r}) d\mathbf{r}$. Here we dropped the subscript m , representing the m^{th} helium atom. This finally gives for the matrix element U_{ij}^{DIM}

$$U_{ij}^{DIM}(\mathbf{r}_I) = \int \rho(\mathbf{r} + \mathbf{r}_I) V_{ij}^{DIM}(r) d\mathbf{r} \quad (2.40)$$

The eigenvalues $U_k^{\text{np}}(\mathbf{r}_I)$ of this real symmetric matrix define the potential energy curves (PECs) without spin-orbit coupling as a function of the distance between the surrounding helium and the impurity for a given helium density.

2.6.2 Including spin-orbit coupling

For the study of the alkali metal Rb in this work, the spin-orbit (SO) splitting of the energy levels is comparable to the splitting of the orbital angular momentum levels $\Lambda = 0$ and $\Lambda = \pm 1$ due to the interaction with the helium. Therefore the spin-orbit interaction needs to be included in the total interaction Hamiltonian.

The total electronic Hamiltonian is given by the sum of the DIM-interaction and the SO-interaction

$$\mathcal{H} = \mathcal{U}^{DIM} + \mathcal{V}^{SO}. \quad (2.41)$$

The SO-matrix is approximated by the atomic alkali one, which is approximated by

$$\mathcal{V}^{SO} = g \mathbf{L} \cdot \mathbf{S} = \frac{1}{2}g(\mathbf{J}^2 - \mathbf{L}^2 - \mathbf{S}^2) \quad (2.42)$$

The coupling constant g is usually approximated by that of the free atom^[69]. We can extend the DIM basis Equation (2.33) to include the projection of the electron spin $s = \{\uparrow, \downarrow\}$ corresponding to the quantum numbers $m_s = \{\frac{1}{2}, -\frac{1}{2}\}$:

$$|p_i, s\rangle \in \{|p_x, \uparrow\rangle, |p_x, \downarrow\rangle, |p_y, \uparrow\rangle, |p_y, \downarrow\rangle, |p_z, \uparrow\rangle, |p_z, \downarrow\rangle\}. \quad (2.43)$$

In this basis the matrix \mathcal{V}^{SO} is given by

$$\mathcal{V}^{SO} = \frac{1}{2}g \begin{pmatrix} 0 & 0 & -i & 0 & 0 & 1 \\ 0 & 0 & 0 & i & -1 & 0 \\ i & 0 & 0 & 0 & 0 & -i \\ 0 & -i & 0 & 0 & -i & 0 \\ 0 & -1 & 0 & i & 0 & 0 \\ 1 & 0 & i & 0 & 0 & 0 \end{pmatrix} \quad (2.44)$$

Kramers' theorem states that the two-fold degeneracy of the levels originating from total half-integer spin cannot be broken by electrostatic interactions^[70]. Therefore all the electronic eigenstates of \mathcal{H} are doubly degenerate. Diagonalising \mathcal{H} yields three doubly degenerate potential energies between the impurity and surrounding helium.

The dynamic evolution of the electronic excited state of the impurity is described by introducing an additional degree of freedom, a 6-component vector $|\lambda\rangle$, which describes the coefficients of the electronic state in the $\{|p_i, s\rangle\}$ basis

$$|\lambda(t)\rangle = \sum_{\substack{i=\{x,y,z\} \\ s=\{\uparrow,\downarrow\}}} \lambda_{is}(t) |p_i, s\rangle \quad (2.45)$$

such that $\|\langle\lambda|\lambda\rangle\|^2 = 1$. The complete set of variables required to describe the system consists of the complex valued effective wave function for helium $\Psi(\mathbf{r}, t)$ with $\rho(\mathbf{r}, t) = |\Psi(\mathbf{r}, t)|^2$, the impurity position $\mathbf{r}_I(t)$, and the 6-dimensional complex vector to determine its electronic wave function $|\lambda(t)\rangle$. The total energy of the impurity-⁴He_N complex after excitation to the ²P manifold is

$$\begin{aligned} E[\Psi, \mathbf{r}_I, \lambda] = & \frac{\hbar^2}{2m_4} \int |\nabla\Psi|^2 d\mathbf{r} + \int \mathcal{E}_c[\rho] d\mathbf{r} \\ & + \frac{1}{2}m_I \dot{\mathbf{r}}_I^2 + \int \rho(\mathbf{r}) V_\lambda(\mathbf{r} - \mathbf{r}_I) d\mathbf{r} + \langle \lambda | \mathcal{V}^{SO} | \lambda \rangle \end{aligned} \quad (2.46)$$

where V_λ is defined as

$$V_\lambda(\mathbf{r}) := \langle \lambda | \mathcal{V}^{DIM} | \lambda \rangle = \sum_{ijss'} \lambda_{is}^* V_{ijss'}^{DIM}(\mathbf{r}) \lambda_{js'} \quad (2.47)$$

and the components of the 6×6 matrix \mathcal{V}^{DIM} given by

$$V_{ijss'}^{DIM}(\mathbf{r}) = V_{ij}^{DIM} \delta_{ss'} = \left\{ V_\Pi(r) \delta_{ij} + [V_\Sigma(r) - V_\Pi(r)] \frac{r_i r_j}{\|\mathbf{r}_m\|^2} \right\} \delta_{ss'} \quad (2.48)$$

The time evolution of the system is obtained by minimising the following action

$$\begin{aligned} \mathcal{A}[\Psi, \mathbf{r}_I, \lambda] = & \int \left\{ i\hbar \int \Psi^*(\mathbf{r}) \frac{\partial}{\partial t} \Psi(\mathbf{r}) d\mathbf{r} + m_I \ddot{\mathbf{r}}_I^2 \right. \\ & \left. + i\hbar \left\langle \lambda \left| \frac{\partial}{\partial t} \right| \lambda \right\rangle - E[\Psi, \mathbf{r}_I, \lambda] \right\} dt \end{aligned} \quad (2.49)$$

Variation of the action \mathcal{A} with respect to $\{\Psi^*, \langle \lambda |, \mathbf{r}_I\}$ yields the following three coupled EL-equations

$$\begin{aligned} i\hbar \frac{\partial}{\partial t} \Psi &= \left[-\frac{\hbar^2}{2m_4} \nabla^2 + \frac{\delta \mathcal{E}_c}{\delta \rho(\mathbf{r})} + V_\lambda(\mathbf{r} - \mathbf{r}_I) \right] \Psi \\ i\hbar \frac{\partial}{\partial t} |\lambda\rangle &= \mathcal{H} |\lambda\rangle \\ m_I \ddot{\mathbf{r}}_I &= -\nabla_{\mathbf{r}_I} \left[\int \rho(\mathbf{r}) V_\lambda(\mathbf{r} - \mathbf{r}_I) d\mathbf{r} \right] = -\int V_\lambda(\mathbf{r} - \mathbf{r}_I) \nabla \rho(\mathbf{r}) d\mathbf{r} \end{aligned} \quad (2.50)$$

where the explicit time dependence of the variables is omitted for clarity. The second line of Equation (2.50) is a 6×6 matrix equation with the matrix elements of \mathcal{H} given by

$$H_{ijss'} = U_{ijss'}^{DIM} + V_{ijss'}^{SO} = \int \rho(\mathbf{r}) V_{ijss'}^{DIM}(\mathbf{r} - \mathbf{r}_I) d\mathbf{r} + V_{ijss'}^{SO} \quad (2.51)$$

In the cases that SO-coupling can be neglected the 6-dimensional electronic state vector $|\lambda\rangle$ reduces to the 3-dimensional vector

$$|\lambda(t)\rangle = \sum_{i=\{x,y,z\}} \lambda_i(t) |p_i\rangle \quad (2.52)$$

and the 6×6 matrix \mathcal{H} reduces to the 3×3 matrix of Equation (2.40) with elements

$$H_{ij} = U_{ij}^{DIM} = \int \rho(\mathbf{r}) V_{ij}^{DIM}(\mathbf{r} - \mathbf{r}_I) d\mathbf{r} \quad (2.53)$$

2.6.3 Absorbing potential at the box boundaries

2.6.4 Technical details on how the dynamic equations are solved

For more details about how this method is implemented the interested reader is directed to Ref. [71]. For the collection of Fortran code that has been used to obtain the results presented here see Ref. [72]. For the manual to use the code, with included example calculations see Ref. [73].

Part I

Photo-excitation dynamics of alkalis

Part II

Capture by quantised vortices

7

Quantised vortices in droplets

Qne of the most unambiguous signatures of the quantum mechanical nature of a substance –and indeed of superfluidity– is the appearance of quantised vortices. The work in this part of the thesis is mostly inspired and motivated by experiments performed by Gomez, Loginov and Vilesov^[13,14].

Normal fluids rotate rigidly when their containers are spinning at low angular velocities, with an angular velocity v_\perp proportional to the distance r from the axis of rotation $v_\perp \propto r$. This behaviour changes completely when the normal fluid is replaced by a superfluid like liquid helium below T_λ ; below a critical angular velocity, the fluid remains at rest. When the angular velocity of the container is increased above this critical velocity, one or more quantised vortices are nucleated. In contrast to a normal fluid, the angular velocity v_s of a superfluid directly outside the vortex core is inversely proportional to the distance from the vortex core $v_s \propto 1/r$. These vortices can be described by an effective wave function and a quantised circulation Γ of the velocity field

$$\Gamma = s \frac{h}{m} \quad (7.1)$$

where s is the angular momentum quantum number, h is Planck's constant and m is the mass of the ${}^4\text{He}$ atom (see Equation (1.29) for a derivation and Refs. [101, 102]). An important aspect in the study of vorticity in finite systems is the energy and momentum transfer between vortices and surface excitations, because they determine nucleation dynamics, shape and the stability of vortices. But the study of quantum vortices is no longer confined to superfluids like liquid helium. Recently^[102,103] it has been extended to BECs confined in magnetic traps. Contrary to confined BECs, superfluid helium droplets are self-contained systems that do not require an external trap to keep them from falling apart. Moreover, they provide an opportunity to study the regime of a strongly interacting quantum system. The width of vortex cores, about 0.2 nm^[101] in superfluid helium-4, is small compared to the size of the droplets (typically a diameter of $\sim 4.4\text{--}10.9$ nm), suggesting a rich variety of three-dimensional phenomena. Quantum vortices in superfluid droplets are therefore a very active field of interest^[104-107].

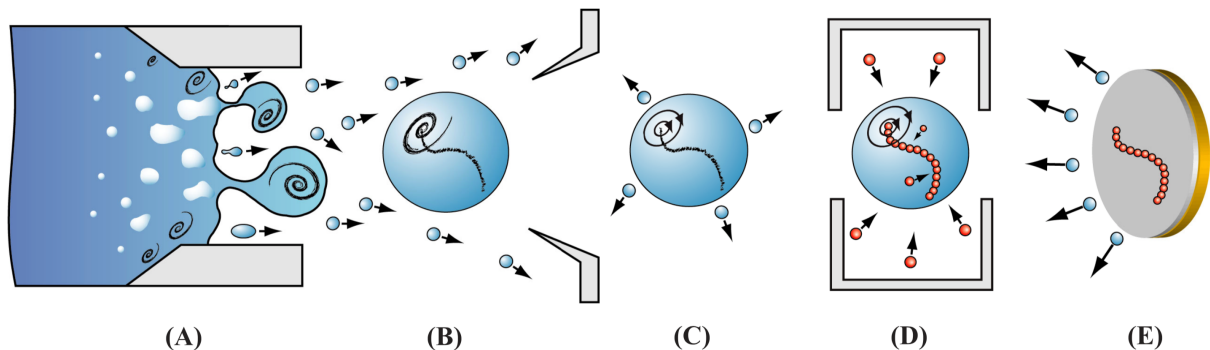


Figure 7.1: Schematic of the experiment. (a) He fluid expands in vacuum and (b) breaks up into rotating droplets. (c) A quantum vortex is formed as a consequence of fast evaporative cooling of the droplet to below T_λ . (d) The droplet is doped with Ag atoms, which are attracted to the vortex core. (e) The droplet then collides with the carbon surface leaving behind the Ag trace, whereas the He evaporates. (Illustration courtesy of Gomez *et al.* 2012, see Ref. [13])

Recently, Gomez *et al.* performed experiments^[13] where vortices inside superfluid ^4He nanodroplets, produced by the expansion of liquid helium, were doped with Ag atoms which then clustered along the vortex lines in the droplets. The helium droplets needed by these kind of experiments need to be larger than the ones used before for single atom spectroscopy and dynamics studies, because they need to be big enough to be able to host an array of vortices, doped with many Ag clusters.

A schematic of the experimental principle is shown in Figure 7.1. Helium droplets are produced by expansion of He, at 20 bars and a temperature $T_0=5.4\text{-}7\text{ K}$, into a vacuum through a nozzle. The droplets cool down rapidly by evaporation and reach a temperature of 0.37 K ^[41]. This temperature is well below the superfluid transition temperature $T_\lambda=2.17\text{ K}$ ^[101,102]. Further along the apparatus, the droplets capture about $10^3\text{-}10^6$ Ag atoms in an oven^[108]. The droplets are then collided against a thin carbon film substrate at room temperature^[108]. When the droplets hit the carbon film they evaporate while leaving behind on the surface the Ag filaments, which are subsequently imaged via a transmission electron microscope (TEM).

The ubiquity of elongated filament-shaped deposits (see Figure 1.5) shows that vortices are present in droplets larger than about 300 nm (about 10^9 atoms) and that their lifetime exceeds a few milliseconds.

Two years later Gomez *et al.* reported^[14] on the formation of quantum vortex lattices inside droplets. They used single-shot femtosecond X-ray coherent diffractive imaging to investigate the rotation of single, isolated superfluid helium-4 droplets containing about $10^8\text{-}10^{11}$ atoms, corresponding to radii of $\approx 100\text{-}1000\text{ nm}$. The formation of quantum vortex lattices inside the droplets was confirmed by observing the characteristic Bragg

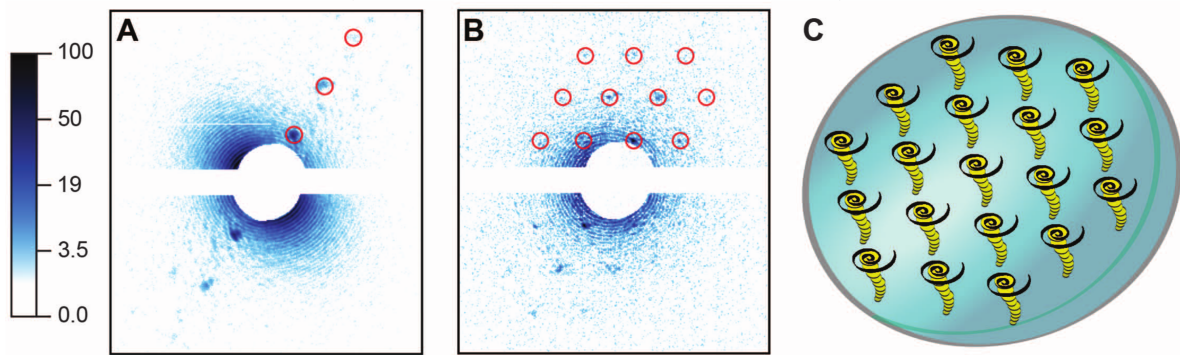


Figure 7.2: He droplets doped with Xe atoms. (A and B) X-ray diffraction images of doped droplets, displayed in a logarithmic intensity scale. (C) Droplet and embedded Xe clusters. Images in (A) and (B) correspond to tilted and parallel alignments of the vortex axes with respect to the incident x-ray beam, respectively. (Illustration courtesy of Gomez *et al.* 2014, see Ref. [14])

patterns from xenon clusters trapped in the vortex cores (see Figure 7.2).

8

Head-on collisions of Xe and Cs¹

8.1 Introduction

It is well established that helium droplets can readily capture in their interior almost any atom or molecule interacting with them, as first shown for the case of Ne atoms^[109], with the notable exception of alkali^[11] and some alkaline-earth^[110] atoms. This property, together with the very low temperature (T) achieved in helium droplets – of the order of 0.4 K – makes them the perfect ultracold and inert environment for hosting and studying isolated atoms and molecules, which is at the basis of current applications of helium droplets for spectroscopic studies of atoms and molecules. Besides, the superfluid nature of helium facilitates binary encounters of atoms/molecules in the bulk of the droplet while absorbing the energy released upon recombination, making possible chemical reactions which would not otherwise occur in the gas phase. These unique properties of helium droplets have had a huge impact on their study^[107,111-114].

The pickup of Ar, Kr and Xe atoms in the gas phase by ${}^4\text{He}_N$ droplets with $N > 10^3$ atoms produced by nozzle beam expansions was studied about twenty years ago by Toennies and coworkers^[115]. In these experiments the droplets in the helium beam were deflected by impacting with a secondary beam made of rare gas atoms in order to detect the pick-up.

Very recently, time-dependent density functional theory (TDDFT) has been used to address the capture of Cs or Ne atoms by ${}^4\text{He}$ nanodroplets^[116,117]. The Cs capture was treated fully three dimensionally with the Cs atom described as a classical particle, whereas for the Ne capture study the Ne atom was described quantum-mechanically but the description was strictly one-dimensional.

¹Published work, see: F. Coppens, A. Leal, M. Barranco *et al*, J Low Temp Phys **187**, 439 (2017).

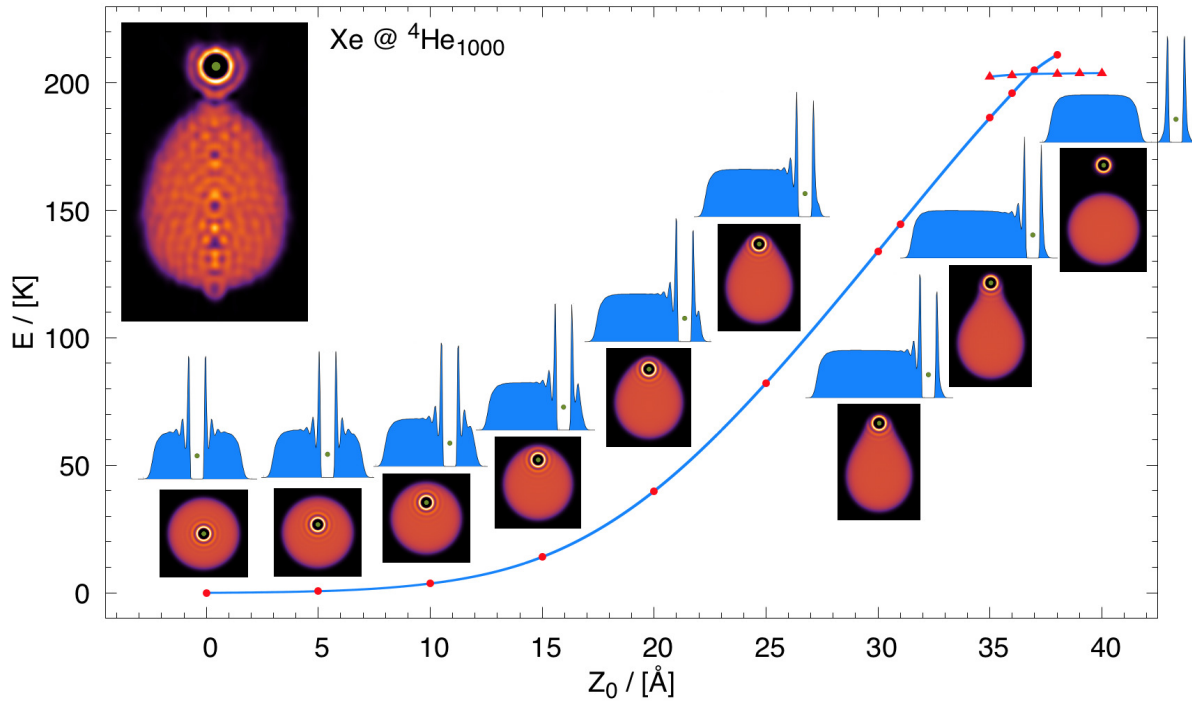


Figure 8.1: Energy of the $\text{Xe}@\text{He}_{1000}$ complex as a function of the distance between the Xe atom and the COM of the droplet. Several two-dimensional helium densities and density profiles are shown for distances between 0 and 40 Å in 5 Å steps. Connected (dots) and disconnected (triangles) helium configurations are shown (see text). Top left inset: Snapshot of the helium density at the first turning point during the dynamic evolution of a Xe atom (green dot) at $v_0 = 600$ m/s attained 78 ps after it has started. (Color figure online.)

Motivated by recent experiments that use Xe atoms to visualise vortex arrays in very large helium droplets^[14,118], we present here a first step towards the description of the capture of Xe atoms by helium droplets, namely head-on collisions of Xe atoms against a He_{1000} droplet. A discussion on the dynamic capture of Xe atoms by droplets hosting vortex lines and vortex arrays will be provided by a forthcoming study combining DFT simulation of vortex arrays as in Refs. [119, 120] for helium nanocylinders and nanodroplets and collision with Xe atoms as in this work. Whenever possible, the results for Xe, a heliophilic atom, are contrasted with results for Cs, a heliophobic atom with similar mass. We use TD-DFT as described in Section 2.6.

8.2 Results

Due to computational constraints we consider a droplet made of $N = 1000$ helium atoms. Its ground state structure is obtained using DFT and gives a sharp-density radius of about

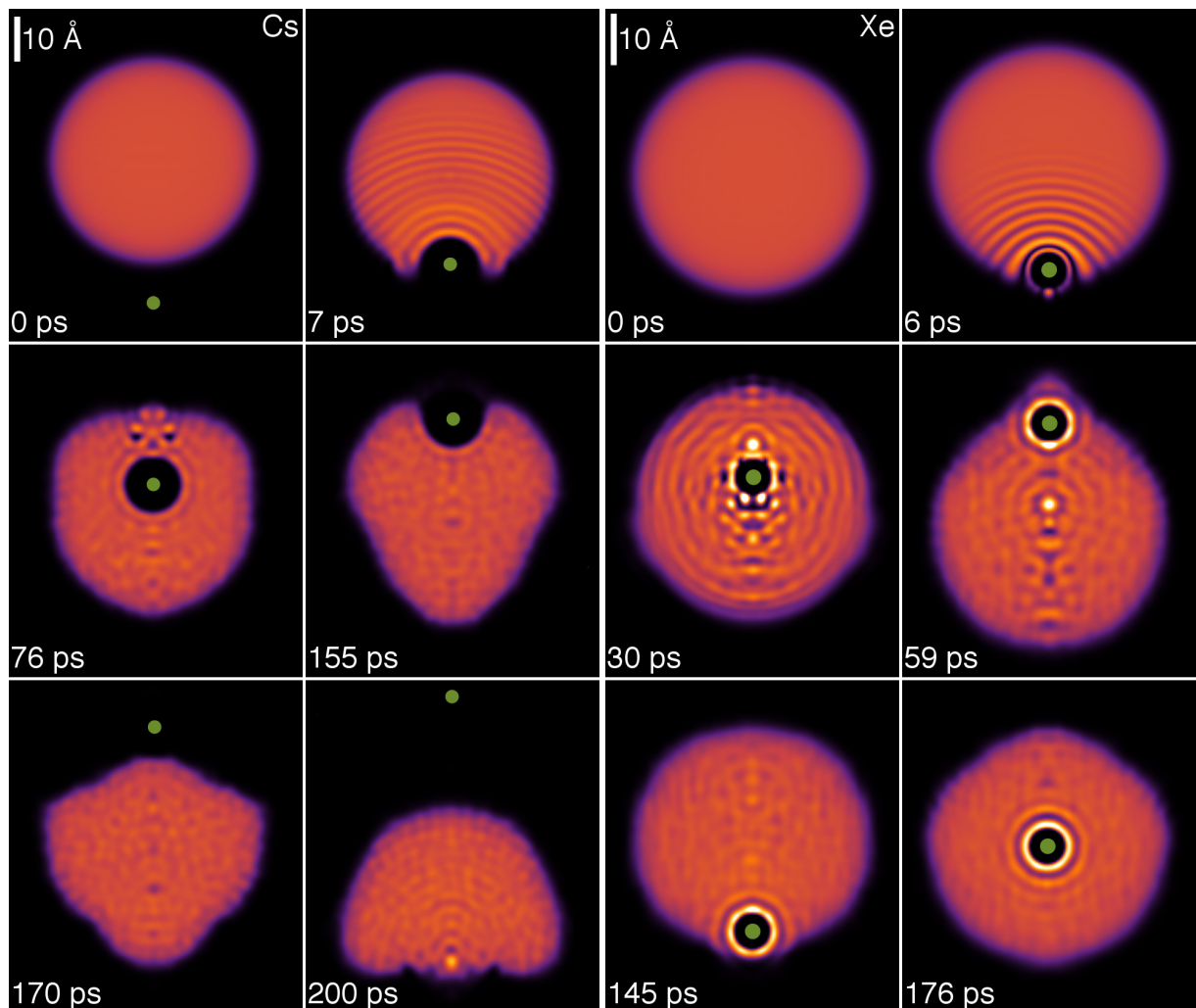


Figure 8.2: Right panel: Dynamic evolution of a Xe atom (big dot) approaching the ${}^4\text{He}_{1000}$ droplet from below at $v_0 = 200$ m/s. The corresponding time is indicated in each frame. Left panel: Same as the right panel, but for a Cs atom. (Color figure online.)

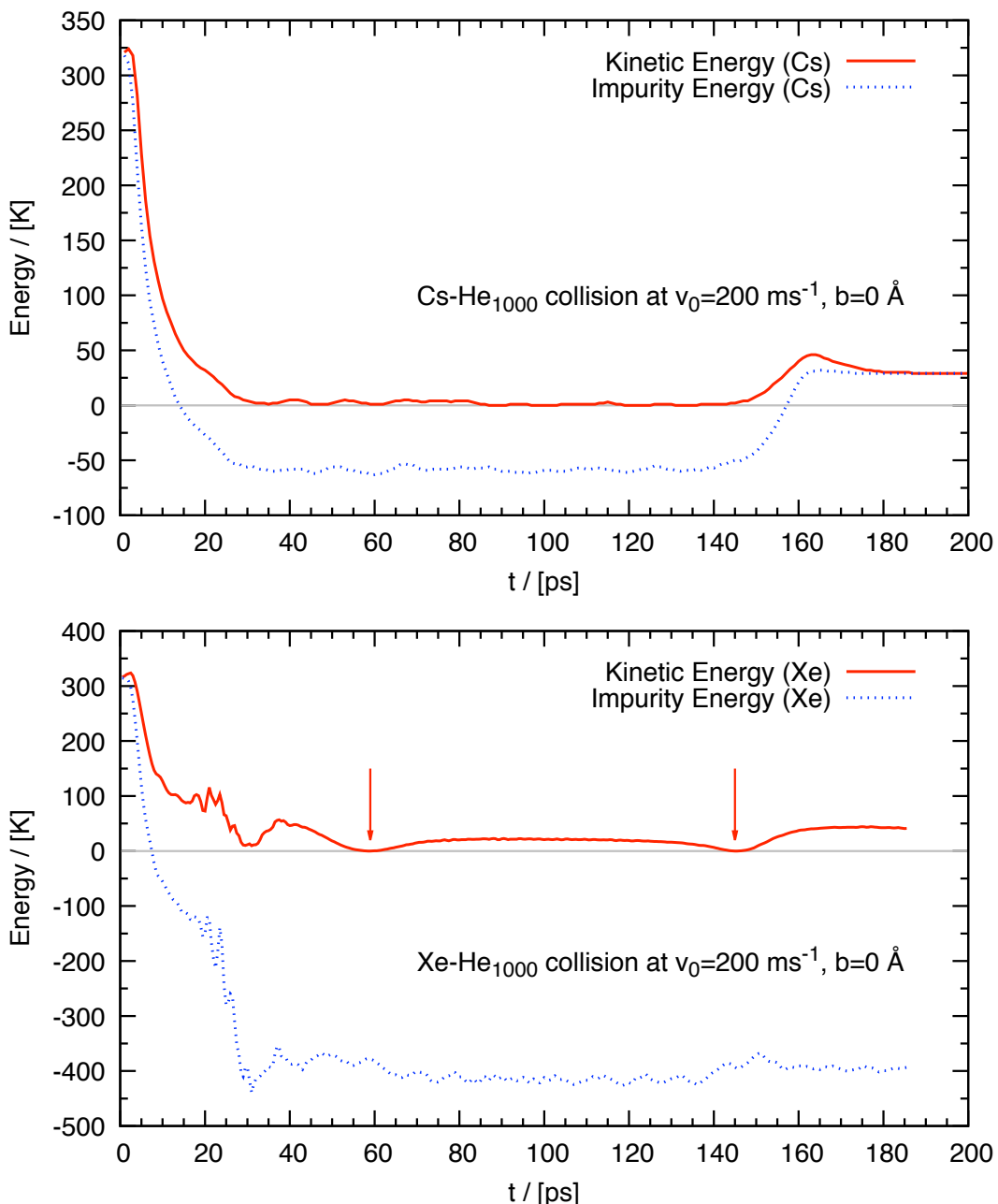


Figure 8.3: Top figure: Kinetic and total (kinetic plus potential) energy as a function of time of a Cs atom head-on colliding against a ${}^4\text{He}_{1000}$ droplet at $v_0 = 200 \text{ m/s}$. Bottom figure: same as top figure for a Xe atom. The vertical arrows indicate the first two turning points at 59 and 145 ps, whose corresponding helium densities are shown in the right Figure 8.2. (Color figure online.)

22.2 Å. Then the dynamics is initiated by placing the Xe atom 32 Å away from the center of mass (COM) of the droplet with an impact parameter equal to zero (head-on collision). The simulations are carried out for initial Xe velocities v_0 ranging from 200 to 600 m/s in the system of reference of the droplet, corresponding to kinetic energies between 315.8 K and 2842 K. These energies can be compared to the solvation energy of a Xe atom at the center of a ${}^4\text{He}_{1000}$ droplet, $S_{\text{Xe}} = E(\text{Xe} @ {}^4\text{He}_{1000}) - E({}^4\text{He}_{1000}) = -316.3$ K. For the sake of comparison, the solvation energy of Cs is -5.2 K and its equilibrium position is in a dimple at the outer droplet surface, about 26.6 Å from its centre.

Thermal Xe atoms ($v_0 \sim 240$ m/s) are used in the experiments^[14,118], and the average droplet velocity is about 170 m/s^[121].

Figure 8.1 shows the energy of the $\text{Xe} @ {}^4\text{He}_{1000}$ complex referred to that of the equilibrium configuration (Xe at the center of the droplet, -5716.4 K) as a function of the distance between the Xe atom and the COM of the droplet. It is obtained by a constrained calculation similar to that presented in Ref. [122] for Ba^+ . With increasing distance, the stretched droplet-Xe configuration eventually breaks into a minicluster around the Xe atom containing about 22 helium atoms disconnected from the rest of the droplet. The appearance of this minicluster is at variance with the situation for a heliophobic impurity such as Cs^[116]. The stretched (connected) configuration energies are represented by dots, the disconnected ones by triangles. The two corresponding curves cross at 37 Å. At shorter distances the connected configuration is stable and the disconnected one metastable, and at larger distances the roles are inverted. In an actual dynamics the number of He atoms in the minicluster depends on the velocity of the Xe projectile.

Figure 8.2 displays two-dimensional plots of the helium density for Xe head-on colliding against the ${}^4\text{He}_{1000}$ droplet at $v_0 = 200$ m/s, and Figure 3 the energy of the impinging atom as a function of time, with the corresponding plots for Cs collisions for the sake of comparison. It can be seen that for both species most of the initial kinetic energy is spent in piercing the droplet surface, after which the impurity moves inside the droplet at a velocity well below the critical Landau velocity v_L .

Figure 8.2 also shows that the collision launches a series of density waves in the droplet that are reflected at the droplet free surface producing complex interference patterns in its bulk. As an illustrative example, Figure 8.4 shows the density profile along the incident direction (z axis) corresponding to the Xe collision at $v_0 = 200$ m/s, 6 ps after the process starts. The wave number associated to this wave can be estimated from the wavelength λ of the oscillations, $q = 2\pi/\lambda \sim 2.7$ Å⁻¹.

In the case of Xe, Figure 8.2 and Figure 3 reveal the appearance of turning points at which the velocity of the impurity is zero. Note that these points are not fixed during the dynamics since the droplet deforms due to the swift motion of Xe inside it; the droplet is not a rigid object and reacts to the motion of the impurity, with energy being transferred

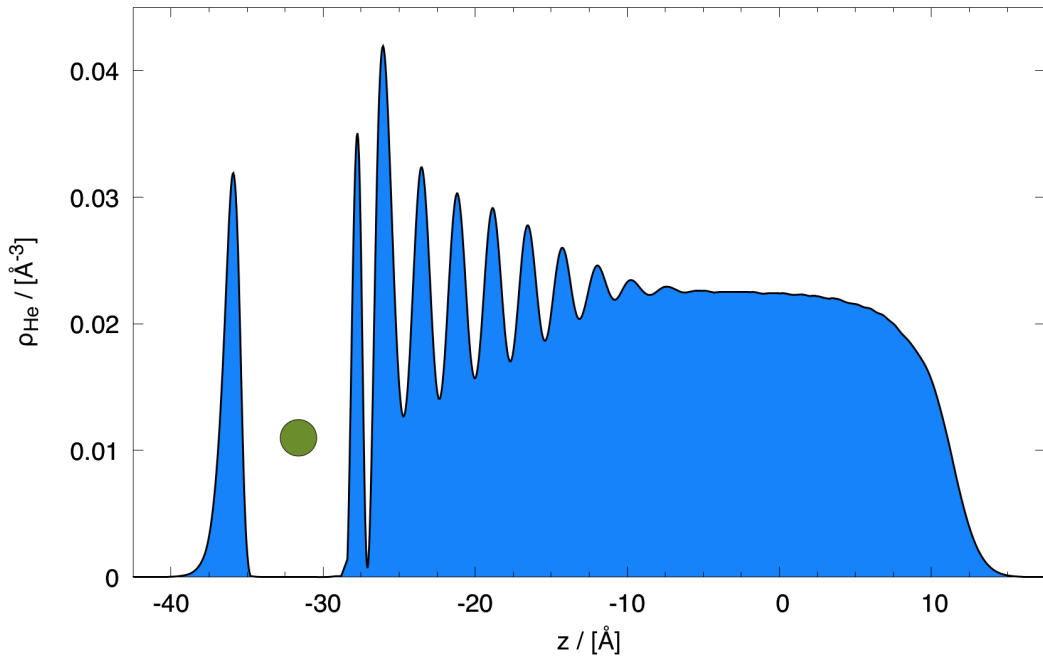


Figure 8.4: Density profile of the He_{1000} droplet along the incident direction corresponding to the Xe collision at $v_0 = 200$ m/s after 6 ps. (Color figure online.)

not only from the impurity to the droplet but also the other way around^[123].

The top left inset in Figure 8.1 shows a snapshot obtained at the first turning point for $v_0 = 600$ m/s, with 57 He atoms around the Xe dopant. We have found that the Xe atom has to hit the droplet at a velocity above 600 m/s in order to go across the helium droplet, otherwise it remains attached to the droplet. The kinetic energy lost by the Xe atom is partially deposited in the droplet and partially carried away by prompt-emitted helium atoms, *i.e.* atoms expelled early on in the collision and with a significant kinetic energy. The number of He atoms emitted during the first 78 ps is about 47. For comparison, about 19 atoms are emitted after 185 ps for $v_0 = 200$ m/s. Eventually, the energy deposited into the droplet should be lost by atom evaporation; however, the time scale for this to happen is beyond the reach of any realistic simulation.

The piercing of the droplet by the Cs atom produces a density wave that travels on its surface and collapses at the surface region opposite to the hitting point. This collapse nucleates a vortex ring (the two dark spots in the 76 ps plot of the left panel of Figure 8.2)^[116].

It is worth pointing out that the falloff of the Xe velocity in the $t = 20 - 30$ ps interval observed in Figure 3 is due to the increase of its inertia as a result of the appearance of a dynamic “snowball” -a crust of helium atoms surrounding the Xe bubble indicated by the bright spots in Figure 8.2- that is eventually washed out at larger times. At variance with our findings for Ba^+ ^[123], vortex rings have not been nucleated in the case of Xe; in

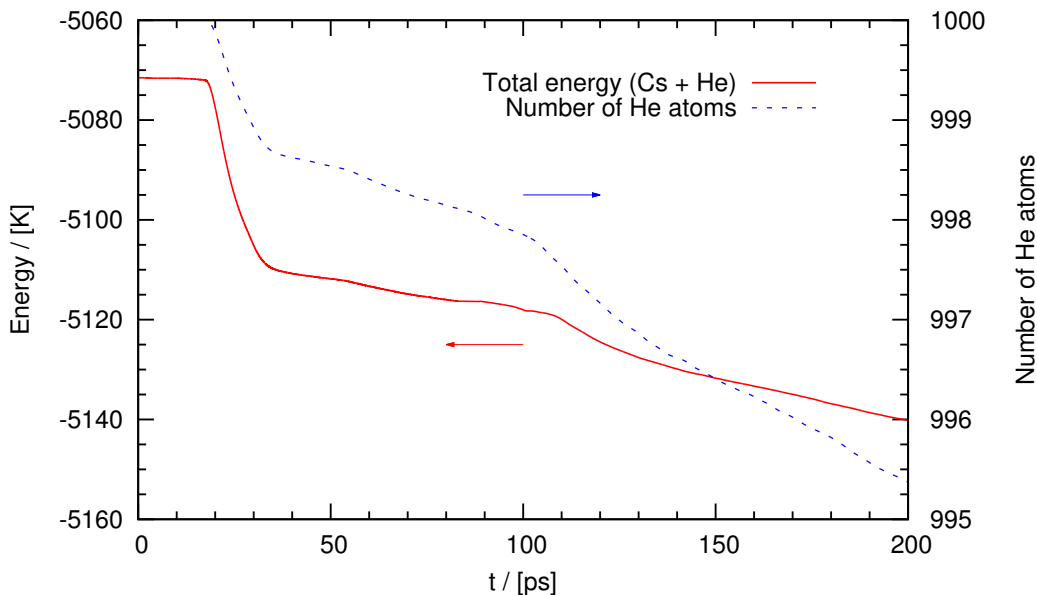


Figure 8.5: Total energy (left scale) and number of atoms in the droplet (right scale) as a function of time for the $\text{Cs}@\text{He}_{1000}$ system at $v_0 = 200$ m/s. (Color figure online.)

particular, we have checked that the two dark spots in the 30 ps plot of the right panel of Figure 8.2 for Xe do not correspond to a vortex ring.

The collapse of the Cs bubble at the surface of the droplet some 150 ps after the process gives back to the impurity part of the kinetic energy it has lost in the piercing of the droplet. The Cs atom is expelled at 64.5 m/s (corresponding to 33.6 K kinetic energy). The number of prompt-emitted helium atoms is 5, which is smaller than for Xe at the same collision energy (19 atoms). As revealed by Figure 8.5, they are preferentially emitted as a forward burst (first sharp drop around 20 ps in the number of atoms) and as a backward burst (second sharp drop slightly after 100 ps).

9

Capture by He droplets hosting quantised vortices¹

9.1 Introduction

As presented in Section 8.1, it is well established that helium droplets can readily capture in their interior almost any atom or molecule interacting with them. Recently, a technique has been introduced to determine the size of large He droplets ($N > 10^5$). It is based on the attenuation of a continuous droplet beam through collisions with Ar atoms at room temperature^[121]. The pickup chamber of the droplet beam apparatus is filled with argon gas and the helium droplets experience multiple, isotropic collisions with the Ar atoms on their way towards the detection chamber.

Large helium droplets could also be doped in this way. This method, using Xe atoms, has been instrumental for detecting and imaging quantized vortex arrays in helium droplets^[14,124]. Xe atoms were used in these experiments because of their large sensitivity to the x-ray coherent diffractive imaging employed to detect them within the helium droplets. Experiments with large superfluid helium droplets are reviewed in a recent publication^[125].

The impurity-droplet interaction in the presence of vortices is also relevant as the first stage of a more complex process leading to the formation of nanowires, see e.g. Refs. [126–129]. Long filaments made of micrometer-sized solid hydrogen particles trapped on quantized vortex cores were used to directly image the vortex reconnection between quantized vortices in superfluid helium^[130].

The impact and capture of impurities interacting with pure helium droplets has been addressed recently within time-dependent density functional theory (TDDFT). Real time simulations have been carried out for heliophobic^[116] (Cs) and heliophilic^[117] (Ne) atoms.

¹ Published work, see: F. Coppens, F. Ancilotto, M. Barranco *et al*, Phys. Chem. Chem. Phys. **19**, 24805–2481 (2017).

In addition to the TDDFT equation for ^4He , heavy impurities are treated as classical particles using Newton's equation of motion, whereas a time-dependent Schrödinger equation has been used in the case of light impurities within the mean field model^[117,131]. A comparison between the results for head-on collisions of Cs and Xe atoms –heliophobic and heliophilic atoms of similar mass– has been presented in Chapter 8 (see Ref. [132] for the published version).

Here we present results obtained within TDDFT for the collision and capture of Xe and Ar atoms by a $^4\text{He}_{1000}$ droplet at different kinetic energies and impact parameters. Special attention is paid to the time-dependent interaction of Xe and Ar atoms with helium nanodroplets hosting vortex lines, and to the effect of multiply-doped vortex arrays in large helium droplets.

Due to the heavy computational cost of the TDDFT simulations presented here, we address only a few facets of the capture process that we consider of experimental relevance rather than carrying out a systematic study of the process. In particular:

- We study the capture of Xe atoms by a ^4He nanodroplet, both for head-on collisions and for different impact parameters, with velocities ranging from thermal values up to several hundred m/s. The results of peripheral collisions with different values of the impact parameter are used to estimate the cross section for the Xe capture.
- We study how a Xe atom dynamically interacts with a droplet hosting a vortex line, under different initial conditions resulting in different velocity regimes of the impurity as it collides with the vortex core: i) a Xe atom initially at rest on the droplet surface and sinking under the effect of solvation forces; (ii) a head-on collision of a moving Xe or Ar atom against the ^4He nanodroplet.
- We study the stationary state of a large $^4\text{He}_{15000}$ droplet hosting a ring of six vortex lines, doped with Ar atoms completely filling all six vortex cores. This is the simplest system that mimics those experimentally described in Ref. [14], where doped vortex arrays embedded in rotating ^4He microdroplets have been imaged.

Multimedia materials accompany this work, showing the real time dynamics of several impact/capture processes described here. These materials are presented in the Electronic Supplementary Information (ESI) of Ref. [15] (see DOI: [10.1039/C7CP03307A](https://doi.org/10.1039/C7CP03307A)). They constitute an important part of this work, since often it is only by viewing how a complex microscopic process unfolds in real time that one can catch important physical details which would otherwise escape in a written account.

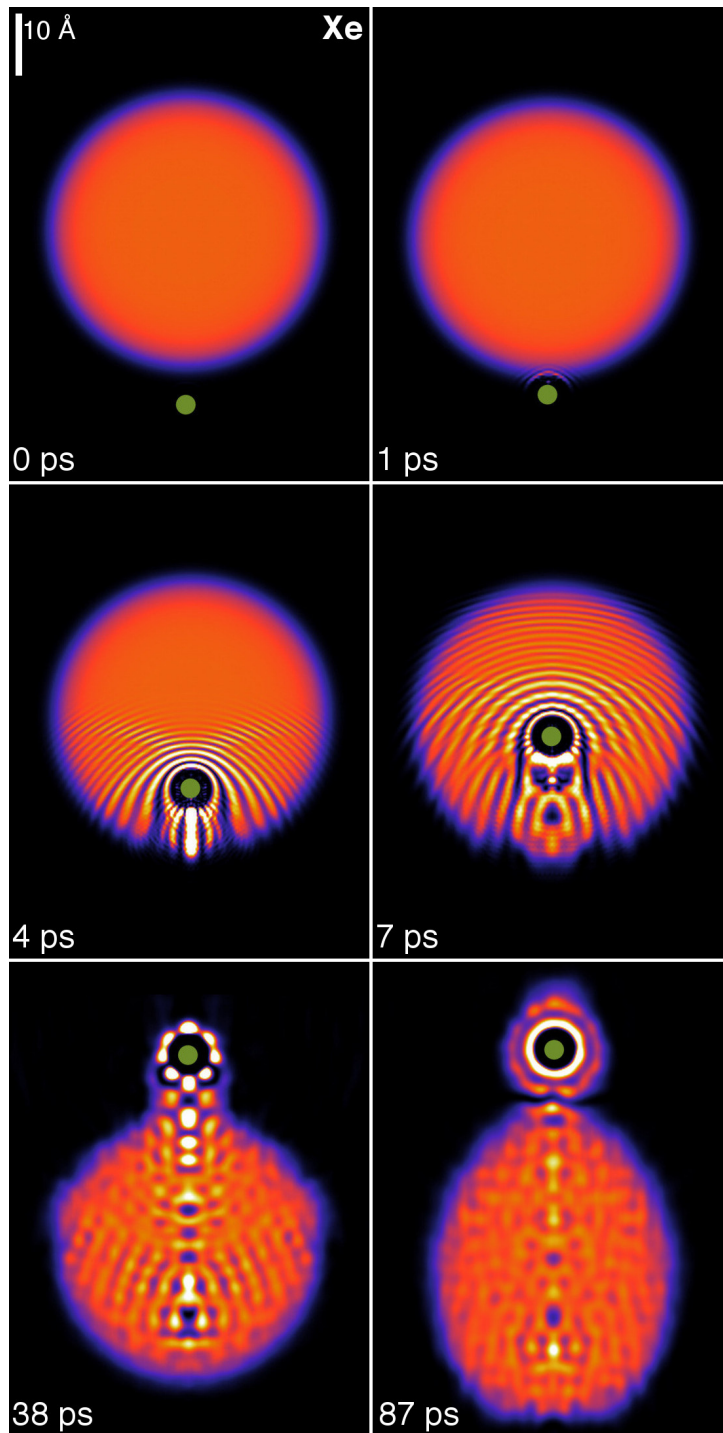


Figure 9.1: Dynamic evolution of a Xe atom (green dot) approaching the ${}^4\text{He}_{1000}$ droplet from below at $v_0 = 600$ m/s. The corresponding time is indicated in each frame. Bright spots correspond to high density regions. (Reproduced from Ref. [15].)

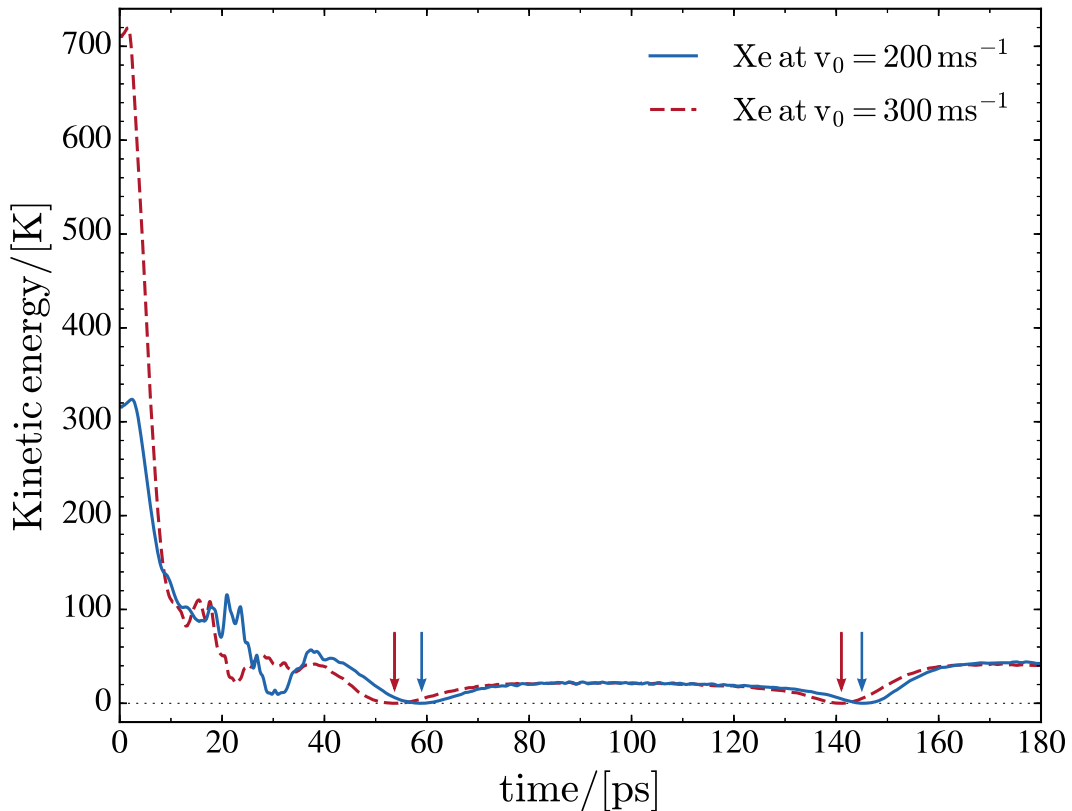


Figure 9.2: Kinetic energy of the Xe atom in the center of mass (COM) frame of the ${}^4\text{He}_{1000}$ droplet as a function of time for a head-on collision at $v_0 = 200$ and 300 m/s. The kinetic energy increase during the first few picoseconds is due to the acceleration produced by the attractive part of the Xe-He potential. The vertical arrows indicate the first two turning points inside the droplet.

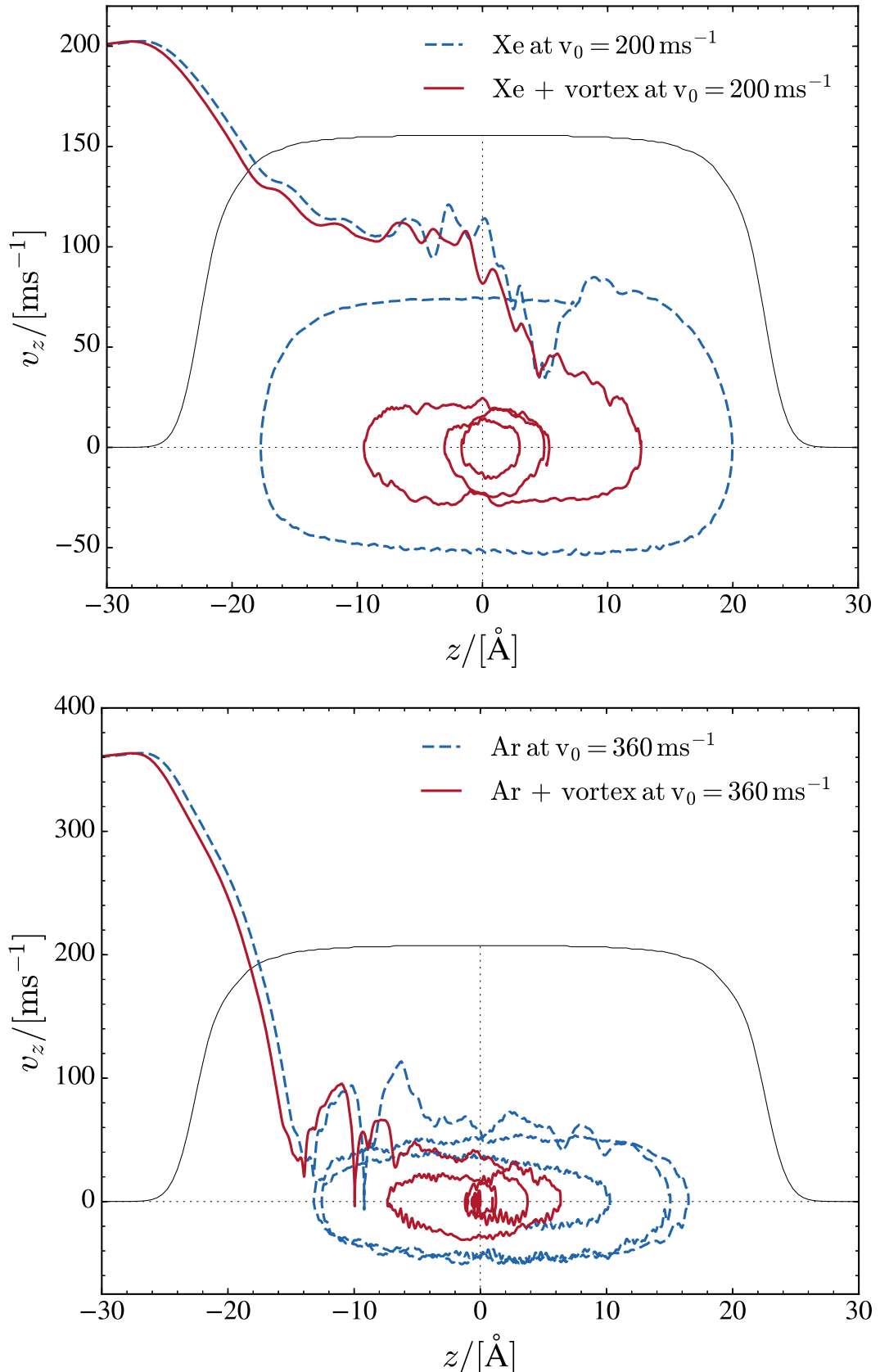


Figure 9.3: Top: Phase-space trajectory of Xe for a head-on collision at $v_0 = 200 \text{ m/s}$ against a ${}^4\text{He}_{1000}$ droplet with and without a vortex line. The Xe atom is referred to the COM frame of the droplet. Bottom: Same as top panel for Ar at $v_0 = 360 \text{ m/s}$. The droplet density at $t = 0$ is also represented in arbitrary scale (black profile)

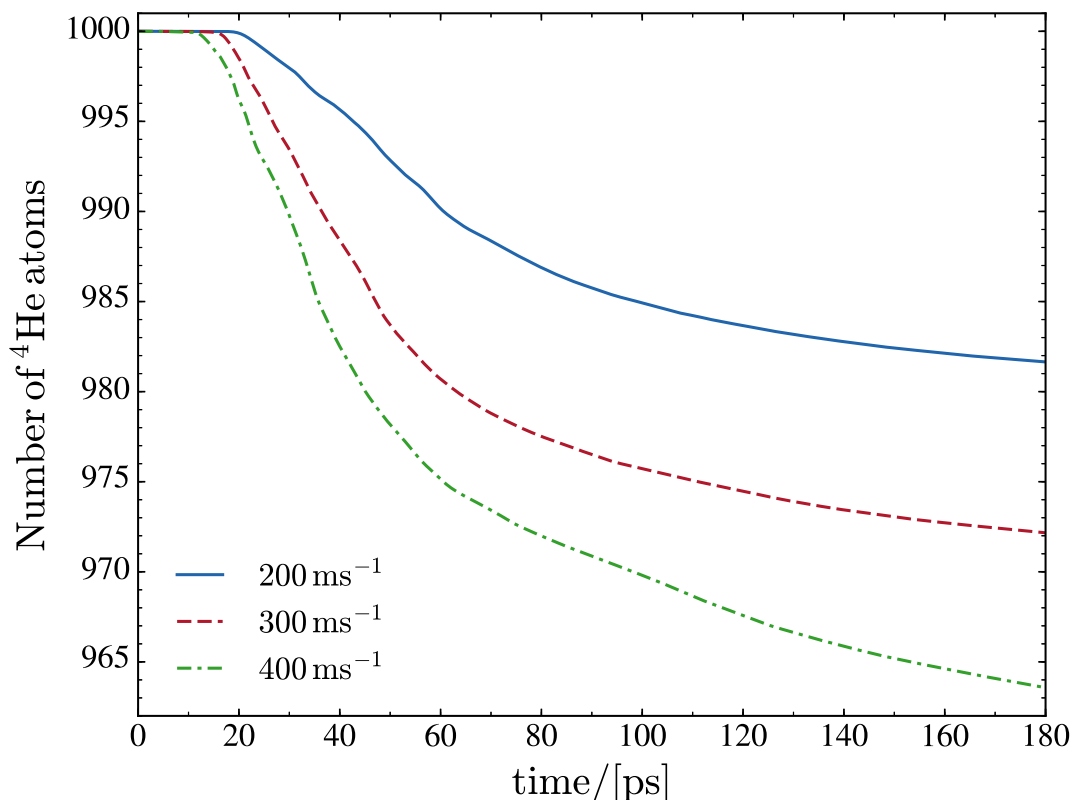


Figure 9.4: Number of He atoms remaining in the droplet as a function of time for the Xe against ${}^4\text{He}_{1000}$ collision at $v_0 = 200, 300$ and 400 m/s .

9.2 Xe capture by vortex-free droplets

We have simulated head-on collisions of a Xe atom with a ${}^4\text{He}_{1000}$ droplet at relative velocities v_0 ranging from 200 to 600 m/s. Figure 9.1 displays two-dimensional plots of the helium density for the highest value, $v_0 = 600$ m/s. This velocity is well above the range of velocities typically encountered in experiments^[14,121,124]. In spite of the appearance of disconnected helium density shown in the $t = 87$ ps frame, we have found that the Xe atom eventually turns around and is captured again inside the droplet even at that relatively high impact velocity. Note that the Xe impurity, even when it temporarily emerges from the bulk of the droplet, appears to be coated with a few ${}^4\text{He}$ atoms, see the configuration at 87 ps.

Figure 9.1 also shows the development of bow waves in the density profile, moving ahead of the impurity at supersonic velocity, and an incipient conic density wave front with its vertex at the Xe bubble. Similar conic shapes, characteristic of supersonic flows, are found when an impurity moves in bulk liquid helium. In the present case the limited size of the droplet and the loss of kinetic energy during the first stages of the collision smooth out this front, making it just barely visible in the figure.

For low initial velocities of the impurity, we find that Xe moves back and forth inside the droplet. The turning points are not fixed, because the droplet deforms due to the displacement of the Xe atom and to the waves that are continuously emitted by the moving impurity (mainly in the direction of its motion), hit the droplet surface, and are reflected back inside it^[132]. This is shown in Figure 9.2 for $v_0 = 200$ and 300 m/s. Thermal Xe atoms ($v_0 \sim 240$ m/s) are used in the vortex imaging experiments^[14,124], and the average droplet velocity as it travels through the pick-up chamber is about 170 m/s^[121], corresponding to relative collision velocities which are within the range investigated here. The kinetic energy gained by the Xe atom after the turning point at 140 - 150 ps is precisely due to the fact that the droplet is not a rigid object and reacts to the motion of the impurity. As a consequence, energy is transferred not only from the impurity to the droplet but also the other way around. We want to emphasize that the droplet experiences large deformations rather than large displacements; the velocity of the center of mass (COM) of the droplet is rather small (below 6 m/s for $v_0 = 200$ and 300 m/s as well) due to the large mass difference between the impurity and the droplet.

We have found that most of the energy is transferred from the Xe to the droplet in the first stages of the collision. This is why, for collisions in this kinetic energy range leading to Xe capture, the motion of the impurity inside the droplet is independent on the initial kinetic energy to a large extent. This is shown in Figure 9.3, which displays the trajectory of Xe (Ar) in phase space for $v_0 = 200$ (360) m/s. The figure also shows similar trajectories in the case where a vortex is present in the droplet; these cases will be discussed later in

Table 9.1: Number of He atoms promptly ejected (N_e) and average energy per ejected atom (E_e) during the first 200 ps.

Species	v_0 (m/s)	N_e	E_e (K)
Xe	200	18	19
	300	28	23
	400	37	30
Ar	360	16	22

this chapter.

The kinetic energy lost by the impurity atom is partly deposited in the droplet, where it produces large deformations and sound waves, and partly carried away by prompt-emitted helium atoms. These are atoms with a significant kinetic energy which are expelled from the droplet early on in the collision process. Figure 9.4 shows the number of atoms remaining in the simulation cell as a function of time for collisions with Xe at $v_0 = 200, 300$ and 400 m/s. Eventually, the energy deposited into the droplet should be lost by atom evaporation. The energy carried away by the ejected He atoms during the first 200 ps is collected in Table 9.1 for the head-on collisions described in this paper. For comparison, the calculated binding energy of a helium atom in the ${}^4\text{He}_{1000}$ droplet is 6.0 K. Note that helium atom ejection continues after 200 ps, the droplet still being far from “thermalized” (equilibrated).

In the case of heavy dopants it is possible to obtain a simple expression for their capture cross section. Defining

$$\kappa = \sqrt{\frac{2\mu E}{\hbar^2}} , \quad (9.1)$$

where μ is the reduced mass of the system and E is the available energy in the center-of-mass frame, and provided that the reduced de Broglie wave length of the impurity $\lambda/(2\pi) = 1/\kappa$ is much smaller than the dimensions of the droplet (which is the case for all v_0 in this study), the system behaves classically and [116]

$$\sigma(E) = \frac{\pi}{\kappa^2} \sum_{\ell=0}^{\ell_{cr}} (2\ell + 1) = \frac{\pi}{\kappa^2} (\ell_{cr} + 1)^2 \quad (9.2)$$

where ℓ_{cr} is the largest relative angular momentum leading to the impurity capture. For a given energy, ℓ_{cr} is determined by carrying out simulations with different impact parameters b using $\ell = \mu v_0 b / \hbar$. We have done it for Xe at $v_0 = 200$ m/s. Figure 9.5 shows the simulation corresponding to the largest impact parameter among the ones we have calculated which led to Xe capture, $b = 20.3$ Å, and Figure 9.6 shows the simulation corresponding to the smallest one which led to Xe deflection, $b = 22.2$ Å. The radius of the droplet, which is defined as $R = r_0 N^{1/3}$ with $r_0 = 2.22$ Å, is 22.2 Å for $N = 1000$. Hence,

at this energy -well within the thermal conditions of the experiment- the cross section for Xe capture is very similar to the geometric droplet cross section.

The circulation lines of the superflow are displayed in two selected panels in Figure 9.5 and Figure 9.6. They show the flow pointing towards the approaching Xe atom at the beginning of the collision and the appearance of vortex loops in the droplet at the latest stages of the simulation. Vortex loops appear from local distortions of the droplet surface^[133]. The circulation lines displayed in the figures of this work have been drawn inside the region where the density is above $0.5 \rho_0$ (with $\rho_0 = 0.0218 \text{ \AA}^{-3}$) that defines the dividing surface of the droplet.

In peripheral collisions not only energy but also angular momentum is deposited into the droplet, which allows to visualize the irrotational flow of the superfluid helium. In particular, for Xe at $v_0 = 200 \text{ m/s}$ and $b = 22.2 \text{ \AA}$ the initial angular momentum is $917 \hbar$. This collision was followed for some 220 ps and produced the ejection of 15 He atoms, 5 of them attached to the Xe atom, see Figure 9.6. After the collision, the $\text{Xe}+{}^4\text{He}_5$ complex carries away 522 angular momentum units, while some 95 units are deposited in the droplet as vortex loops and capillary waves^[134], see bottom right panel of Figure 9.5 and Figure 9.6. The remaining angular momentum is taken away by the ejected helium atoms.

9.3 Helium droplets hosting vortex lines

To determine the structure of a droplet hosting a singly-quantized linear vortex we have started the imaginary time iteration from a helium density in which the vortex is “imprinted”. For this purpose, a vortex line along the z can be described by the effective wave function

$$\Psi_0(\mathbf{r}) = \rho_0^{1/2}(r) e^{i S(\mathbf{r})} = \rho_0^{1/2}(\mathbf{r}) \frac{(x + iy)}{\sqrt{x^2 + y^2}} \quad (9.3)$$

where $\rho_0(\mathbf{r})$ is the density of either the pure or the impurity-doped droplet without vortex. Vortex lines along other directions passing through a chosen point can be imprinted as well^[135].

In the case represented by Equation (9.3), if the impurity is within the vortex core along a symmetry axis of the impurity-droplet complex, the effective wave function $\Psi_0(\mathbf{r})$ - before and after relaxation - is an eigenvector of the angular momentum operator $\hat{L}_z = -i \hbar \partial/\partial \theta$. The angular momentum of the droplet is then

$$\langle \hat{L}_z \rangle = \langle \Psi_0(\mathbf{r}) | \hat{L}_z | \Psi_0(\mathbf{r}) \rangle = N \hbar \quad (9.4)$$

Different energy balances involving pure and doped droplets hosting vortices are defined^[120,135,136]:

- Solvation energy of the impurity:

$$S_X = E(X@{}^4\text{He}_N) - E({}^4\text{He}_N)$$

- Vortex energy:

$$E_V = E(V@{}^4\text{He}_N) - E({}^4\text{He}_N)$$

- Binding energy of the impurity to the vortex:

$$B_X = S_X - \{E[(X + V)@{}^4\text{He}_N] - E(V@{}^4\text{He}_N)\}$$

Using the functional of Ref. [65] and the He-rare gas pair potentials of Ref. [137], solvation energies of -316.3 K and -215.7 K have been found for Xe and Ar atoms, respectively. Thus, for the same incident kinetic energy, about 100 K of additional energy have to be dissipated in the case of Xe in order to get the same kinematic conditions than for Ar.

The binding energy of the impurity to the vortex is the result of a delicate balance between terms which are individually much larger than their difference. It can thus be affected by relatively large inaccuracies. Within DFT, it has been found that the Xe atom is barely bound to the vortex line, with $B_{Xe} \sim 3 - 5$ K^[119,136].

A critical angular velocity ω_c exists above which nucleation of vortices with quantized velocity circulation in units of h/m_4 occurs. The critical angular velocity for nucleating a vortex line along a diameter in a droplet made of N helium atoms is

$$\omega_c = \frac{1}{\hbar} \frac{E_V}{N} \quad (9.5)$$

This expression is obtained by computing the energy that minimizes $\langle H - \omega L_z \rangle$ (*i.e.* corresponding to the equilibrium configuration in the corotating frame) with and without a vortex line^[138]. Using the values appropriate for a ${}^4\text{He}_{1000}$ droplet we obtain $\omega_c = 0.127$ K/ $\hbar = 0.0167$ ps⁻¹.

When the angular velocity is increased above ω_c , larger amounts of angular momentum may be stored into the superfluid by increasing the number of nucleated vortices. The higher the angular velocity, the more packed the vortex array is around the rotation axis. These vortices arrange themselves into ordered structures whose existence in bulk superfluid ${}^4\text{He}$ was established long ago^[139,140].

To generate vortex arrays we have worked in the fixed-droplet frame of reference (corotating frame at angular velocity ω), *i.e.* we look for solutions of the following EL equation:

$$\{\mathcal{H}[\rho] - \omega \hat{L}_z\} \Psi(\mathbf{r}) = \mu_4 \Psi(\mathbf{r}), \quad (9.6)$$

In this case, $\Psi(\mathbf{r})$ no longer is an eigenvector of the angular momentum. To determine $\Psi(\mathbf{r})$ describing a configuration where n_v vortex lines are present we have followed again the imprinting strategy, starting the imaginary-time evolution of Equation (9.6) with the

helium effective wave function

$$\Psi_0(\mathbf{r}) = \rho_0^{1/2}(\mathbf{r}) \prod_{j=1}^{n_v} \left[\frac{(x - x_j) + i(y - y_j)}{\sqrt{(x - x_j)^2 + (y - y_j)^2}} \right] \quad (9.7)$$

where $\rho_0(\mathbf{r})$ is the density of the vortex-free droplet and (x_j, y_j) is the initial position of the j -vortex linear core with respect to the z -axis of the droplet (note that in Refs. [119, 120] $\Psi_0(\mathbf{r})$ was incorrectly written). We underline the fact that during the functional minimization of the total energy, the vortex positions and shapes will change to provide at convergence the lowest energy vortex configuration for the given value of the angular velocity ω .

Figure 9.7 shows the two-vortex stationary configuration of a ${}^4\text{He}_{1000}$ droplet in the corotating frame at angular frequency $\omega = 0.175 \text{ K}/\hbar = 0.0229 \text{ ps}^{-1}$. The angular momentum of this configuration is $\langle \hat{L}_z \rangle = 1836 \hbar$. Notice the bending of the vortex line so that they meet the droplet surface perpendicularly at both ends, and also the flattening of the droplet in the z direction due to centrifugal forces.

At variance with the single vortex line along the symmetry axis of the droplet, the two-vortex configuration is not stationary in the laboratory frame, where the density and velocity field change with time. To show this, $\Psi(\mathbf{r})$ has been evolved in the laboratory for about 150 ps taking as initial condition the stationary configuration in the corotating frame. As expected, the vortex cores appear to rotate in the laboratory frame. Within the numerical accuracy, they do so rigidly. This can be seen in Figure 9.7. Besides, they rotate precisely at $\omega = 0.0229 \text{ ps}^{-1}$. This is a stringent test on the accuracy of the dynamics and the consistency of the method. It can be seen in the ESI material how the two vortex lines turn around each other.

Figure 9.7 shows how a superfluid droplet hosting a vortex array “rotates”. The fact that the vortex cores rotate rigidly is not in contradiction with the irrotational character of the superfluid flow, since they are empty. The cores carry along with them the superfluid whose velocity field is irrotational, whereas for a rigid solid or a classical liquid in steady flow one has $\mathbf{v} = \omega \times \mathbf{r}$, hence $\nabla \times \mathbf{v} = 2\omega$. The circulation lines in Figure 9.7 do not correspond to a rigid rotation, but to an irrotational flow in the presence of two vortices. The helium density adapts to the vortex cores as they rotate and this gives the appearance of a solid rotation in the laboratory frame, but it is not.

It is worth discussing the different configurations that may appear when $\omega < \omega_c$. The lowest energy corresponds to the current-free (CF) $\langle L_z \rangle = 0$ configuration. Metastable one-vortex (1V) configurations with $\langle L_z \rangle = N\hbar$ also exist in this angular frequency range^[119,120]. Other irrotational (IR) configurations with $\langle L_z \rangle < N\hbar$ do exist, arising from velocity potentials such as e.g. $S(\mathbf{r}) = \alpha xy$. For an ellipsoidal droplet with a sharp surface, the parameter α is related to the angular velocity around the z -axis and the deformation of the ellipsoid, see the Appendix and Refs. [141–143].

These *IR* configurations may be generated by using the phase $S(\mathbf{r}) = \alpha xy$ in Equation (9.3) and minimizing $\langle H - \omega \hat{L}_z \rangle$. At a given value of $\omega < \omega_c$, the energies in the corotating frame are ordered as $E_{CF} < E_{IR} < E_{1V}$. Figure 9.8 shows the stationary configuration in the corotating frame corresponding to $\omega = 0.10 \text{ K}/\hbar = 0.0131 \text{ ps}^{-1}$. Although this angular frequency is close to ω_c , this configuration is hardly distorted and hosts a negligible amount of angular momentum: less than $5 \times 10^{-2} \hbar$, compared to the value of $10^3 \hbar$ at ω_c). The circulation lines can be analytically calculated if the density profile is approximated by that of an ellipsoid with constant density, see the Appendix.

Figures similar to Figure 9.8 are shown in Refs. [141, 142] for a rotating elliptic vessel filled with a fluid whose flow is irrotational. Whereas in the case of a rigid solid or viscous liquid in steady flow the entire system rotates as a whole, an irrotationally flowing fluid in a rotating vessel is just pushed by the walls of the container; the same happens for a Bose-Einstein condensed gas in a rotating trap^[143]. For an isolated self-bound ${}^4\text{He}$ droplet, the apparent “rotation” of the system in the laboratory arises from deformations of the fluid elements constituting the droplet, but not from their local rotation which is forbidden by the irrotational condition. The vorticity Ω (defined in hydrodynamics as^[144] $\Omega = \nabla \times \mathbf{v}(\mathbf{r})$), initially distributed in the helium droplet when it is in the normal phase, concentrates in the vortex lines when the droplet becomes superfluid and its velocity field becomes irrotational.

The above discussion shows how difficult is to set a superfluid droplet in rotation. Experimentally^[14, 124, 145] the situation is different, since the helium droplet is initially in a normal phase state at a temperature above the normal-to-superfluid transition temperature T_λ (about 2.17 K in bulk liquid at 1 bar). As a consequence, it may store large amounts of angular momentum and experience large deformations. Copious evaporation drives the droplet into a superfluid state at a temperature below T_λ and the angular momentum remaining in the droplet is then stored in vortex arrays that are being nucleated.

9.4 Dynamics of Xe and Ar capture by vortex lines

To study the interaction of an atomic impurity with vortices, we have imprinted a vortex line in the ${}^4\text{He}_{1000}$ droplet and prepared the Xe atom in different kinematic conditions.

The inelastic scattering of xenon atoms by quantized vortices in superfluid bulk helium has been addressed in Ref. [146]. It was found that a head-on collision leads to the capture of Xe by the vortex line for $v_0 = 15.4 \text{ m/s}$, but not for $v_0 = 23.7 \text{ m/s}$. We have carried out an equivalent simulation by initially placing the Xe atom inside the droplet 10 Å away from the vortex line and sending it head-on towards the vortex at a velocity of 10 m/s. This velocity is of the order of the thermal velocity of a Xe atom in a droplet under experimental conditions, once the droplet has thermalized after capturing the Xe

atom ($T \sim 0.4$ K)^[111]. Since the equilibrium position of the Xe atom is at the center of the droplet, it moves to this region and remains there during the rest of the simulation. In this region of the droplet, the Xe atom is also attracted by the vortex, but it is deflected by the superfluid flow around the vortex line and ends up orbiting around it. Hence it is captured by the vortex without getting into its core.

A detailed analysis of the Xe capture as a function of the impact parameter has also been carried out in Ref. [146], with the conclusion that when the impact parameter of the Xe atom approaching the vortex line is larger than about 5 Å, Xe is deflected but not captured^[146]. In the case of droplets, the final result is very different. Upon capture, the Xe atom wanders erratically inside the droplet, as we have seen in the case of vortex-free droplets. The surface of the droplet deforms dynamically and acts as a “pinball machine”, which eventually brings the Xe atom close enough to the vortex line if it missed it in the first attempt or was not previously ejected off the droplet.

The smoothest capture process one might think of corresponds to the Xe atom being initially placed at rest on the droplet surface, as no kinetic energy is given to the impurity. The Xe atom is accelerated towards the center of the droplet due to the attractive He-Xe interaction. We show that, under these kinematic conditions, some He atoms are first drawn towards the impurity because they are lighter, see also Figure 4, Figure 9.10 and the Electronic Supplementary Information available at doi: [10.1039/C7CP03307A](https://doi.org/10.1039/C7CP03307A) for the continuous movie corresponding to the simulation. Eventually, the impurity with its “solvation structure” sinks, acquires some velocity, and is also deflected by the velocity field of the vortex line.

We have tried two different initial locations of the Xe atom on the droplet surface. One is a point on the equator of the droplet, in a plane perpendicular to the vortex line; the other location is one of the open vortex core ends. Our aim was to see if a sensible difference in the transit time of Xe across the droplet could be detected. The simulations do not show important differences between the time taken by the impurity to reach the center of the droplet. It is about 20 % larger when Xe starts from the equator than from the core end^[15]. It is worth noting that in the latter case the sliding of the impurity along the core proceeds rather smoothly, and that the impurity oscillates back and forth much as in the vortex-free case.

The simulation of Xe ($v_0=200$ m/s) and Ar ($v_0=360$ m/s) atoms head-on colliding with a ${}^4\text{He}_{1000}$ droplet perpendicularly to the vortex line has been analyzed and compared with the result corresponding to a vortex-free droplet. The trajectory of the Xe and Ar atoms in phase space is shown Figure 9.3. In both cases the trajectory of the impurity is limited to the region of the droplet around the vortex line. The impurity orbits around the vortex line because the superfluid flow does so. Since in the DFT approach no dissipation is included, the signature of the capture of an impurity by a vortex is its close orbiting

around the vortex line, as shown in the figure and especially in Ref. [15]. The ESI material shows that whereas Ar is captured during its first transit across the droplet, the Xe atom is only captured in its second transit. We attribute this difference to the larger solvation energy of Xe (see Section 9.3), which requires more time to be dissipated. It can be seen^[15] that when Xe detaches from the vortex in the first transit, the vortex line is reconnected near the atomic solvation structure because no open ends can remain in the bulk of the droplet.

Figure 4 and Figure 9.10 show that when the impurity hits the droplet surface a series of surface and volume density waves are launched. These waves travel much faster than the impurity itself, which has lost a large amount of kinetic energy when it pierced the surface.

The displacement of the atom in the droplet produces sound waves in the liquid and distortions along the vortex line (Kelvin modes). It is worth seeing that before the bending by the collision with the impurity, the vortex line is twisted (helical Kelvin mode). This is due to the interference between the spherical wave front flow produced by the hitting of the droplet surface, that travels from bottom to top, and the flow around the vortex core. The spherical wave front hits first the central portion of the vortex line, whose ends are anchored on the droplet surface. This yields the appearance of the helical distortion along the vortex line shown in Figure 9.11. The twisting can no longer be followed after the impurity solvation structure reaches the vortex line, bending and dragging it along in the course of its orbiting around it. But it is clearly visible before as shown in Figure 9.11, that displays the density of the droplet around the vortex line at the indicated collision time.

We have thus shown that Xe and Ar atoms are readily captured by vortex lines in helium droplets under conditions prevailing in the experiments^[14,124]. Simulating the capture of a huge number of impurities or clusters by vortex arrays in very large droplets is beyond reach at present. However, the results presented in this subsection are the proof of concept that the limitation is technical and not conceptual.

9.5 Vortex arrays in ^4He droplets doped with Ar atoms

The existence of ordered vortex lattices inside ^4He droplets has been established by the appearance of Bragg patterns from Xe clusters trapped inside the vortex cores in droplets made of $N = 10^8 - 10^{11}$ atoms (corresponding to radii from 100 to 1000 nm)^[14,124]. We have recently studied the stability of vortex arrays made of up to $n_v = 9$ vortices inside a ^4He nanodroplet using the DFT approach^[120]. It was found that the energetically favored structure for $n_v > 6$ is a ring of vortices encircling a vortex at the center of the droplet. For $n_v = 6$, the configuration with a six-vortex ring is found to have almost the

same energy as the five-fold ring plus a vortex at the center. The former structure has been experimentally observed^[14,124,145], although classical vortex theory predicts for it a much higher free energy cost than for the latter^[147]. Similar equilibrium structures have been obtained within DFT for helium nanocylinders hosting vortex arrays^[119].

In the experiments of Ref. [124] the diffraction images show that rotating ^4He nanodroplets of about 200 nm in diameter contain a small number of symmetrically arranged quantum vortices whose cores are filled with regularly spaced Xe clusters. Unexpected large distances of the vortices from the droplet center ($\sim 0.7\text{-}0.8$ droplet radii) are observed and explained as a result of the balance between the contribution of the Xe atoms to the total angular momentum of the droplets and the solvation potential of the embedded Xe atoms, which opposes the migration of vortices towards the droplet surface and their annihilation there, as it would happen instead in the case of undoped vortices for low values of the droplet rotational frequency.

In practice, as more and more Xe atoms become attached to a vortex, they adopt the angular velocity of its revolution about the droplet center. If the Xe capture is isotropic, the total angular momentum of the droplet is conserved, and thus the angular momentum accompanying the Xe rotational motion must be transferred from the vortices to the impurities. This reduction in the angular momentum of the vortices causes them to move outwards, resulting in the larger equilibrium distances of the vortices observed in the experiments. The actual equilibrium radial positions result from a balance between this tendency to move towards the droplet surface and the solvation potential, which tends instead to draw impurities towards the droplet center.

We have looked for stationary configurations of a 6-vortex ring in a rotating He_{15000} droplet by solving the EL equations in the corotating frame with a fixed angular velocity. Each vortex core is filled with Ar atoms, and the system is allowed to fully relax. In the end, the column of atoms inside each vortex core reaches an equilibrium structure where the Ar atoms are separated by a distance which is roughly that of the Ar dimer. One such configuration is shown in Figure 9.12. Note that the vortex cores are almost straight lines, whereas in an undoped droplet rotating with the same velocity the vortex lines would be bent, as shown e.g. in Figure 9.7. The Ar atoms are not shown in the Figure. The localized structures appearing in the vortex cores are regions of highly inhomogeneous, high ^4He density resulting from the Ar-He attractive potential.

The presence of impurities thus confers rigidity to the vortex lines, preventing them from bending. Yet, the small segment of the vortex line free from impurities bends so as to hit the droplet surface perpendicularly, see the bottom Figure 9.12. Note that in the absence of vortices, Ar atoms initially placed in a linear chain structure would relax towards the lower energy, compact configuration of an Ar cluster in the bulk of the droplet. However, once trapped by a vortex core, their collapse into such a cluster structure does not occur,

i.e. an energy barrier appears and prevents the formation of Ar clusters. Our simplified description of the more complex experimental conditions (where each vortex line hosts chains of regularly spaced atomic clusters, instead of chains of single atoms) is due to computational limitations.

Our choice of Ar instead of Xe as a dopant is motivated by the weaker He-Ar and Ar-Ar interactions, which facilitates the imaginary-time relaxation. The interaction of the helium environment with several close-by impurities increases the strength of dopant-droplet interaction, producing helium localization around the impurities (snowball structures), see Figure 4. Stabilizing these structures is extremely time consuming, especially when the He-impurity interaction is strong. Experiments were also carried out with Ar atoms as dopants, but have not been analyzed yet. However, no significant difference is expected between argon and xenon, neither from the experimental nor from the theoretical viewpoint.

There are obvious differences in scales between our simulations and the actual experiments, due to computational cost. In experiments heavier impurities are used (Xe), the droplets are much larger and the doping is known to occur by filling the vortex cores with a chain of equally spaced Xe clusters, each made of hundreds of atoms, instead of atom chains as done in our simulations. In spite of these differences, we find results which qualitatively explain the unusual behavior of vortex lines experimentally observed in doped rotating helium droplets.

We have looked for the equilibrium structure of the Ar@6-vortex ${}^4\text{He}_{15000}$ droplet for different imposed values of the angular velocity of rotation. The results show that the doping inside each vortex core adds a substantial stability to the system, such that doped vortices are still stable in a droplet rotating at rather low values of the angular velocities, whereas undoped vortices for such values would be pushed towards the surface of the droplet and eventually expelled. The solvation potential effect becomes apparent below some critical value of the angular velocity, where the vortices cease to move towards the surface and the system reaches an equilibrium maximum distance of the vortices from the droplet center. This is shown in the Figure 9.13, where we plot the radial distance of the vortices from the center as a function of the angular momentum of the system. Note how doped vortices are stable for values of the angular momentum well below the stability limit of an undoped droplet. A similar behavior has been observed in the experiment (see for instance Figure 2 in the Supplemental Material of Ref. [124], see DOI: [10.1103/PhysRevB.93.180510](https://doi.org/10.1103/PhysRevB.93.180510)).

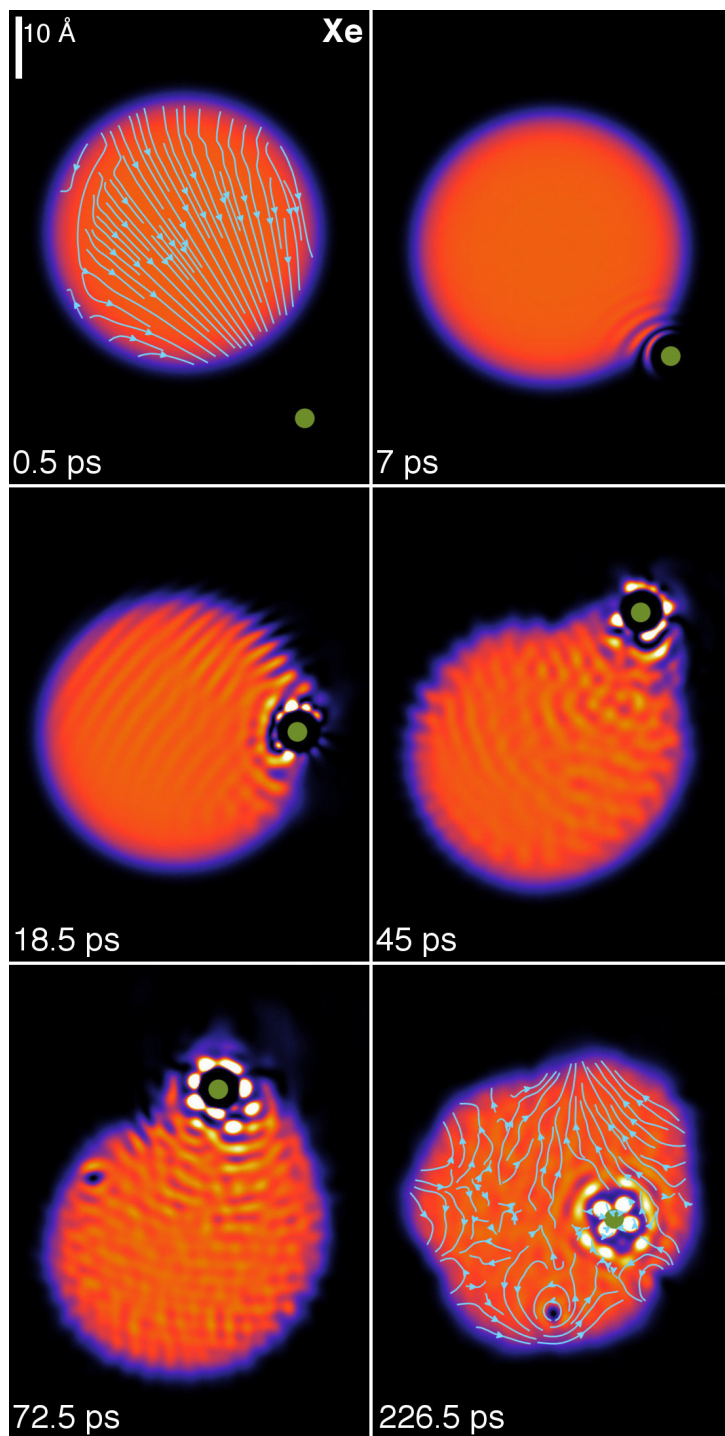


Figure 9.5: Dynamic evolution of a Xe atom (green dot) approaching the $^4\text{He}_{1000}$ droplet from below at $v_0 = 200$ m/s with impact parameter $b = 20.3$ Å. The corresponding time is indicated in each frame. The velocity fields are represented in cyan in the panels at 0.5 ps and 226.5 ps. The bright spots are high He density blobs appearing around the Xe atom because of the attractive He-Xe interaction. See the ESI^[15] for the movie of the complete evolution.

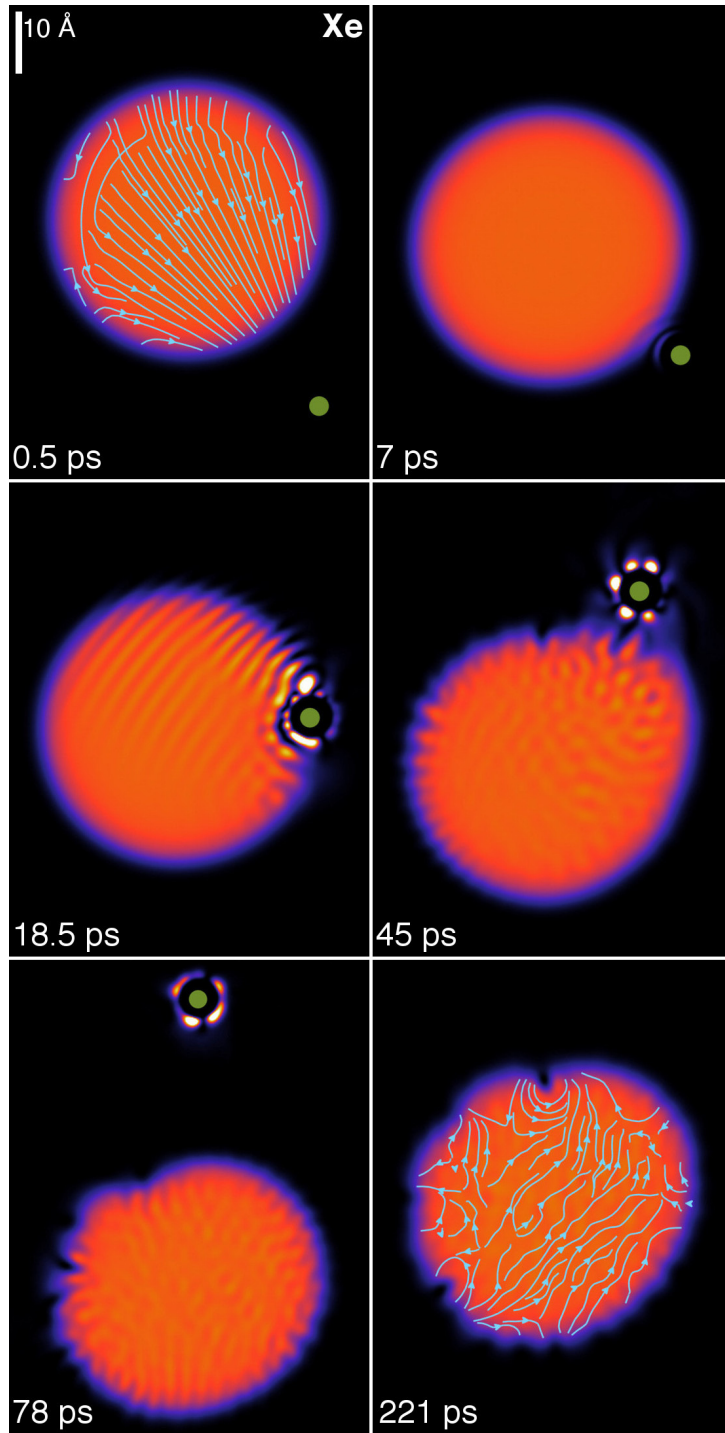


Figure 9.6: The same process as in Figure 9.5 but with an impact parameter $b = 22.2 \text{ \AA}$ instead of $b = 20.3 \text{ \AA}$. Note that in this case, after about 78 ps (bottom left panel), the Xe atom is ejected with some helium density attached to it. See the ESI^[15] for the movie of the complete evolution.

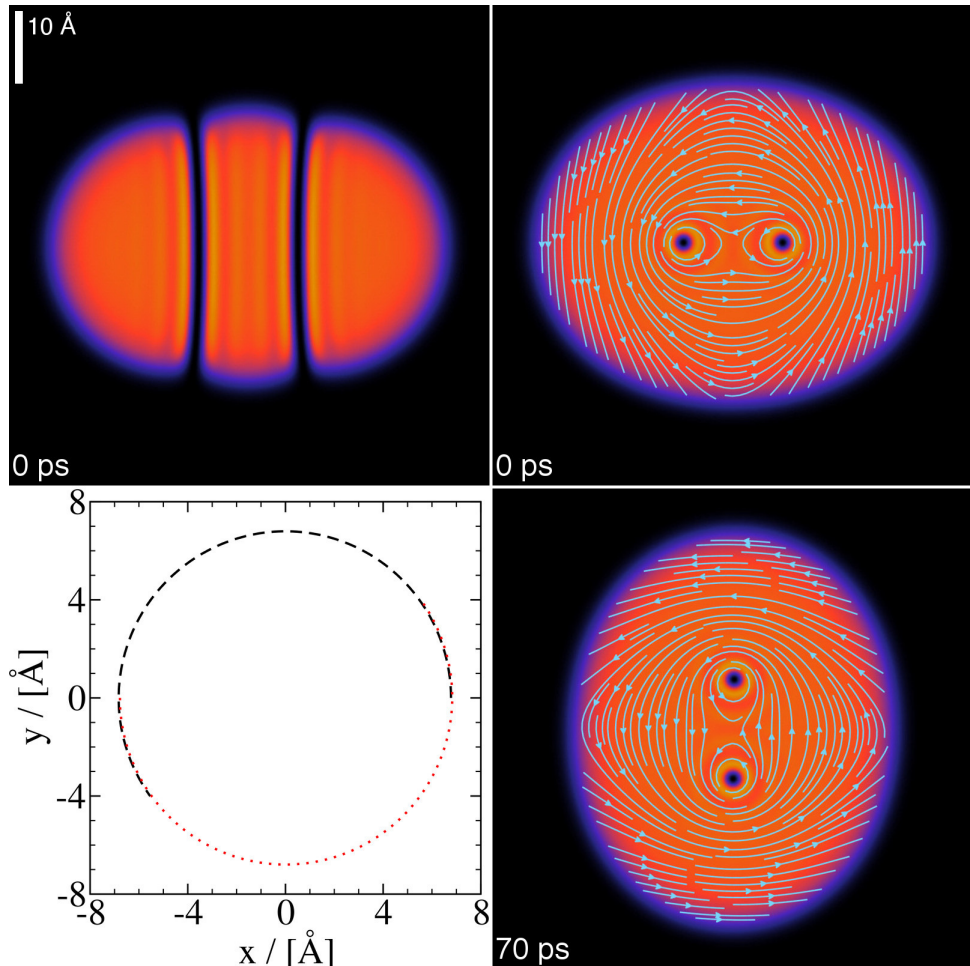


Figure 9.7: $^4\text{He}_{1000}$ droplet at $\omega = 0.0229 \text{ ps}^{-1}$: Top panels, stationary two-vortex configuration on the $x - z$ plane (left) and $x - y$ plane (right) in the corotating frame. Bottom left panel, trajectory of the vortex cores in the $x - y$ plane of the laboratory frame. The dashed line is the trajectory of one of the vortex cores, and the dotted line that of the other. Both trajectories overlap and show that the vortex cores rotate rigidly and this is also visualised by the velocity field lines shown in the right two panels. Bottom right panel, helium density in the $x - y$ plane at $t = 70$ ps obtained in the laboratory frame starting from the above configuration^[15].

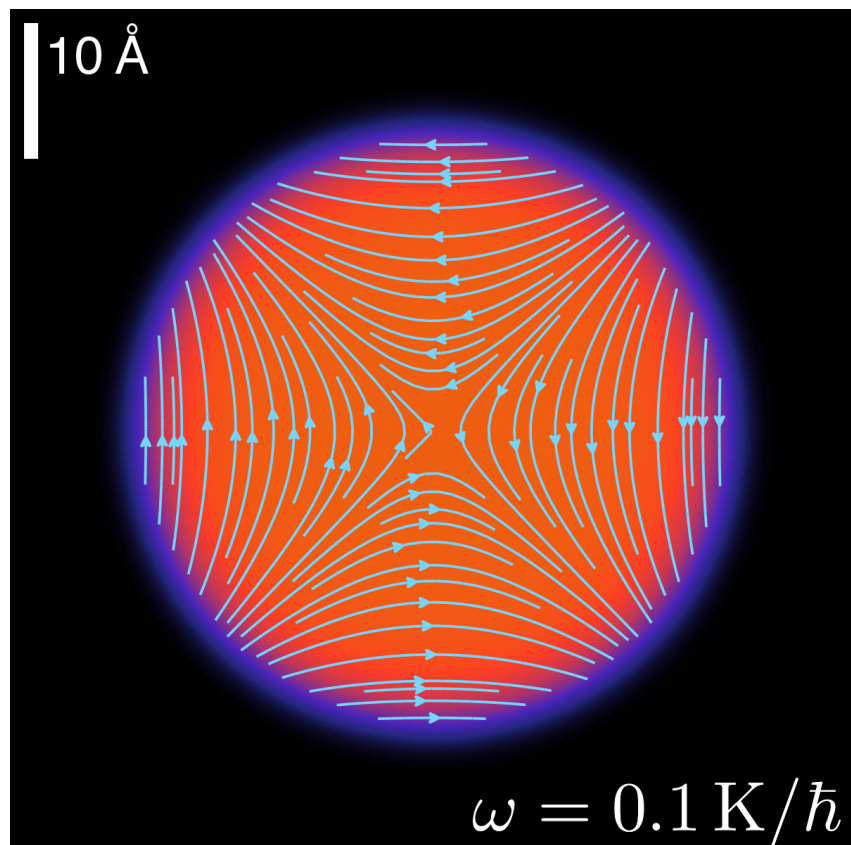


Figure 9.8: Stationary configuration of the ${}^4\text{He}_{1000}$ droplet at $\omega_c \gtrsim \omega = 0.10 \text{ K}/\hbar = 0.0131 \text{ ps}^{-1}$ in the corotating frame ($x - y$ plane). Superimposed is the irrotational velocity field arising from a velocity potential of the form $S(\mathbf{r}) = \alpha xy$.

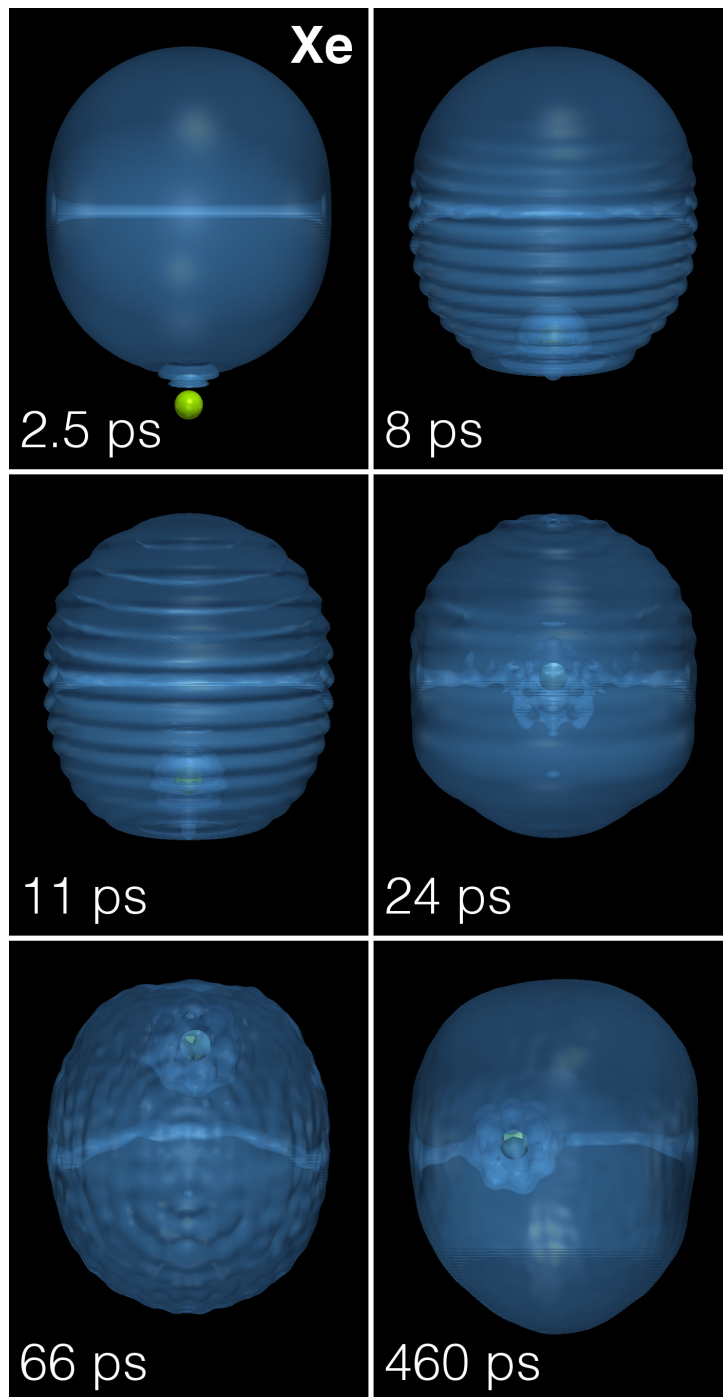


Figure 9.9: Dynamic evolution of a Xe atom (green dot) approaching a ${}^4\text{He}_{1000}$ droplet hosting a vortex line from below at $v_0 = 200$ m/s. The corresponding time is indicated in each frame^[15].

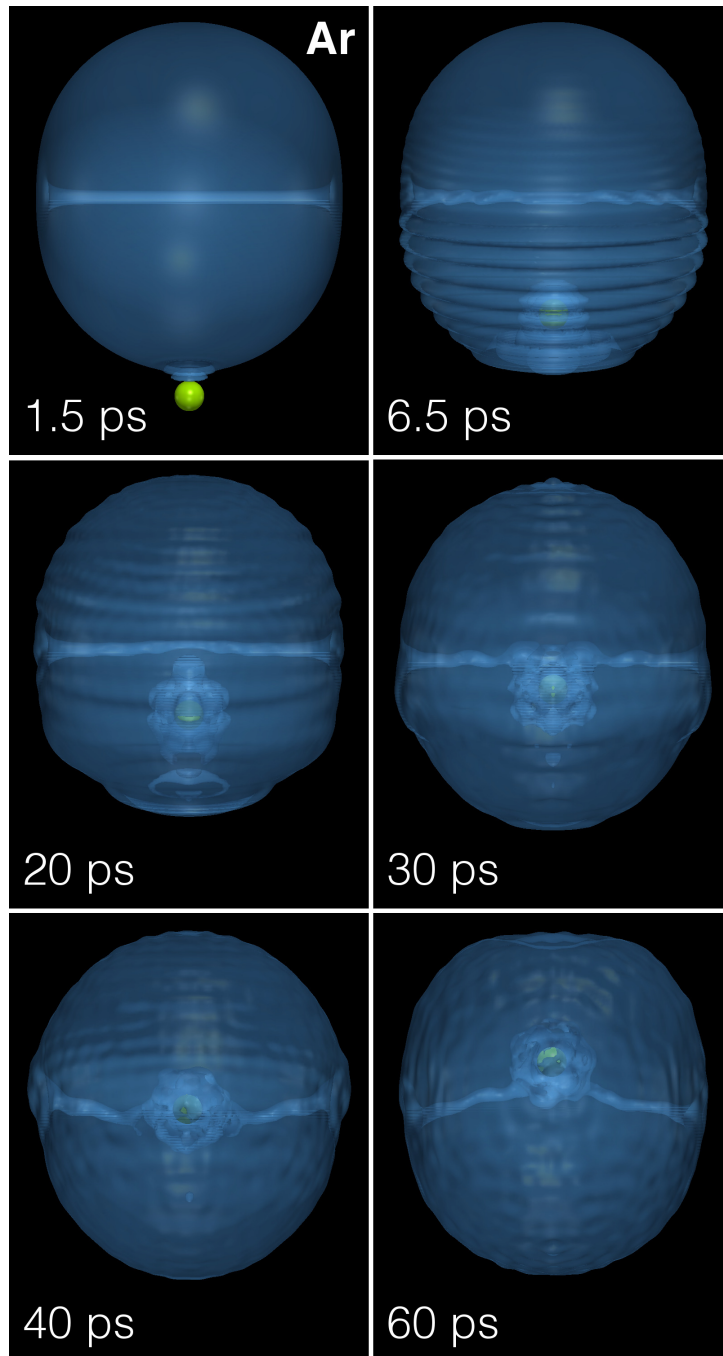


Figure 9.10: Same as Figure 4 for an Ar atom at $v_0 = 360 \text{ m/s}$ ^[15].

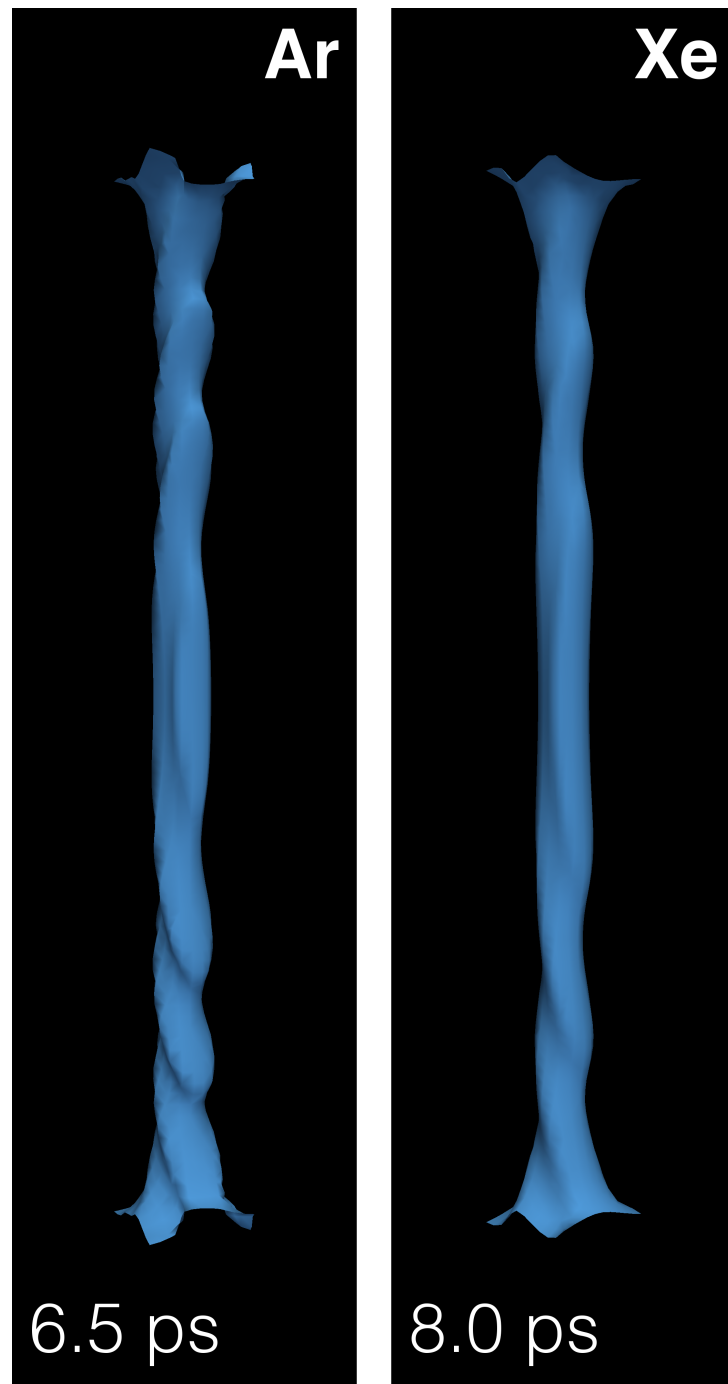


Figure 9.11: Core structure of the vortex line in a ${}^4\text{He}_{1000}$ droplet after colliding with Xe at $v_0=200$ m/s (right panel, $t = 8$ ps) and Ar at 360 m/s (left panel, $t=6.5$ ps). The full structure of the droplet is shown in Figure 4 and Figure 9.10.

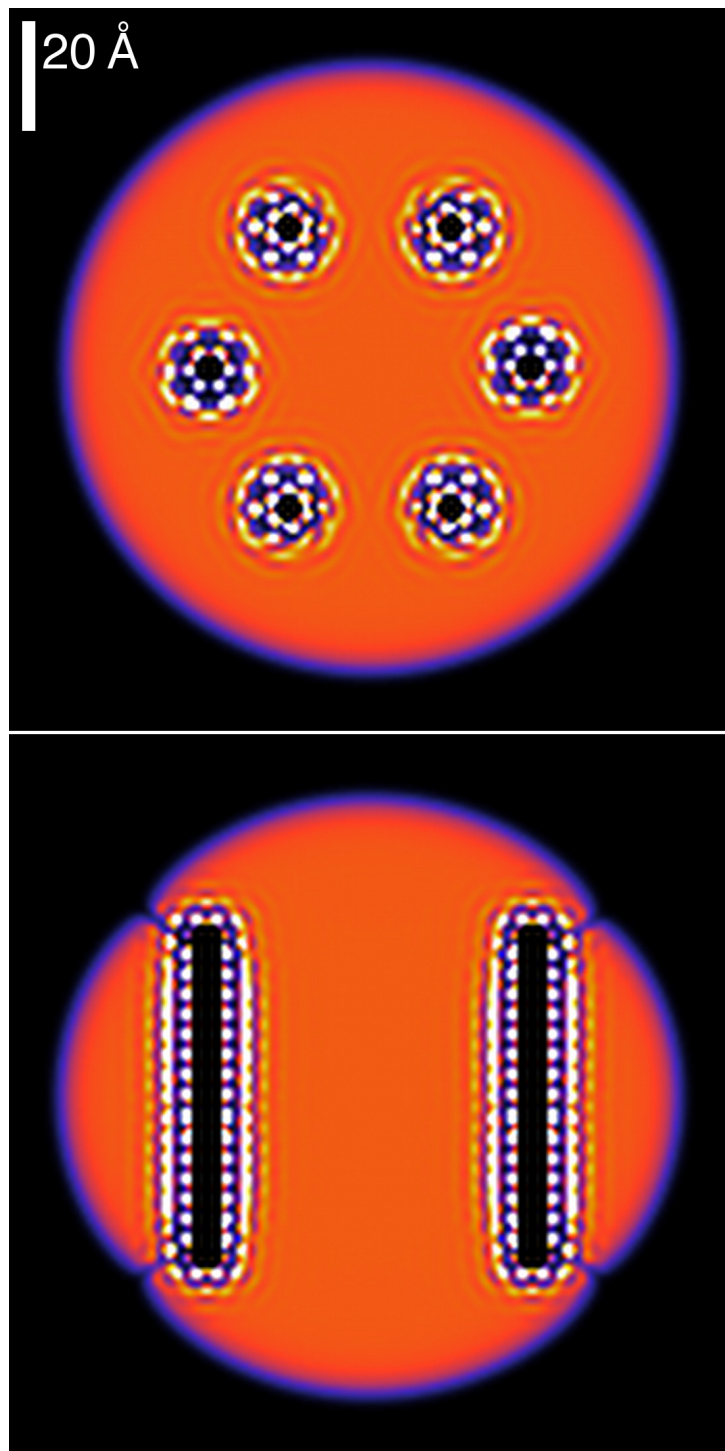


Figure 9.12: Helium droplet configuration hosting six vortices, each doped with a line of regularly spaced Ar atoms (not represented). The top figure shows the density in the $x - y$ symmetry plane (top view), while the bottom figure shows a side view corresponding to the $y - z$ plane. As in some of the previous figures, the bright spots are high density blobs appearing around the impurity atoms.

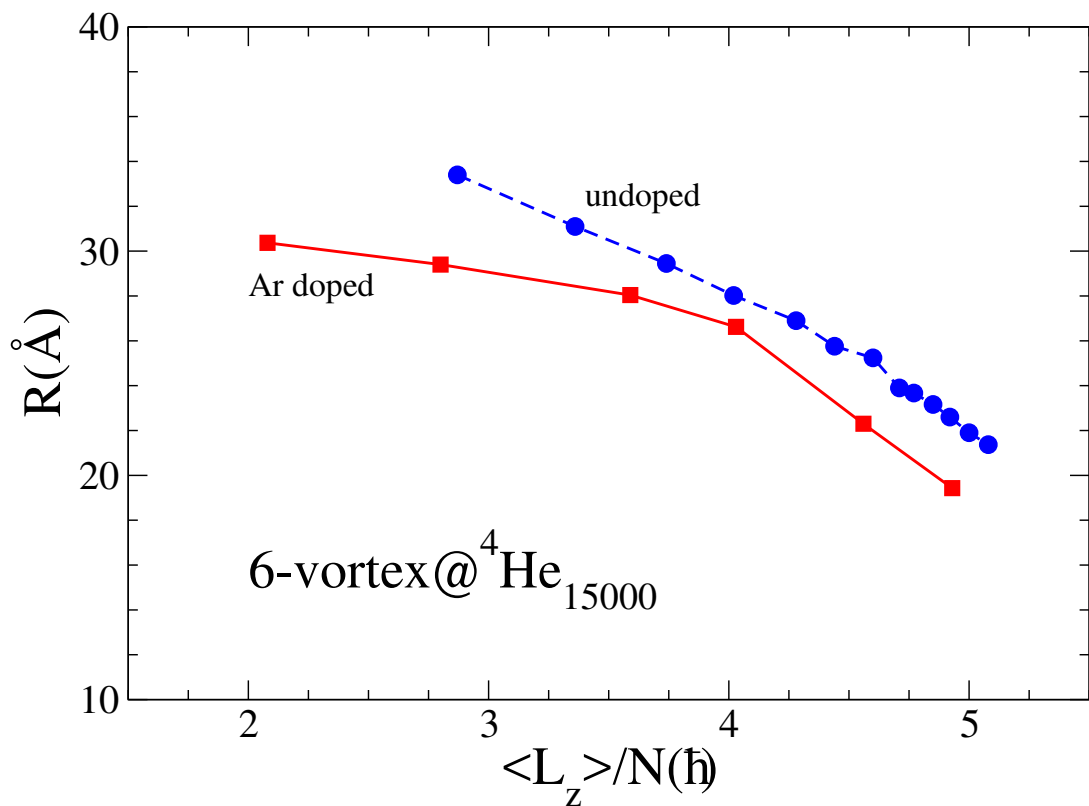


Figure 9.13: Calculated equilibrium distance of the 6-vortex ring from the droplet center as a function of the angular momentum per He atom in units of \hbar . The dots represent the results for undoped vortices, while the squares are the results for Ar-doped vortices. The lines are drawn as a guide to the eye.

